



ORIGINAL RESEARCH ARTICLE

On the Prediction of Flow Stress Behavior of Additively Manufactured AlSi10Mg for High Temperature Applications

Saurabh Gairola, Gaurav Singh, and R. Jayaganthan

Submitted: 10 May 2023 / Revised: 23 March 2024 / Accepted: 30 March 2024

The high-temperature deformation behavior of laser powder bed fabricated (LPBF) AlSi10Mg alloy was investigated using an isothermal hot compression test over a wide range of deformation conditions (150–300 °C and 0.01–1 s⁻¹). Different phenomenological models, namely the Johnson–Cook model, modified Johnson–Cook, strain-compensated Arrhenius equation, modified Zerilli–Armstrong model, modified Fields–Backofen model and artificial neural network (ANN) with feed-forward back propagation learning algorithm, were used for predicting the flow stress dependency on strain, strain rate, and temperature. The accuracy of the predictive capability of these models was determined using different statistical parameters such as correlation coefficient (*R*), average absolute relative error, and root mean square error. The modified Fields–Backofen model and strain-compensated Arrhenius model were identified as the best-suited models for predicting the flow stress behavior of additively manufactured AlSi10Mg, with an average error of 3.3% and 3.9% and correlation coefficient of 0.96 and 0.97, respectively. The ANN model exhibited the highest accuracy in predicting the hot deformation behavior of LPBF-fabricated AlSi10Mg, with an average error of 0.5% and a correlation coefficient of 0.99.

Keywords additive manufacturing, AlSi10Mg, artificial neural network, flow stress, hot deformation

1. Introduction

Additive manufacturing (AM), or 3D printing, is an emerging net-shape manufacturing technology used to produce highly critical components. It is particularly valuable for low-volume productions and mass customization in industries such as aerospace, automotive, and biomedical (Ref 1–3). Laser powder bed fusion (LPBF) is one of the most widely used metal additive manufacturing techniques due to its capability to provide high surface finish, excellent accuracy and highly dense components. This process ensures better mechanical properties and functional properties due to the fine microstructure obtained from the high thermal gradient of additive manufacturing (Ref 4–8). Aluminum silicon alloys (Al–Si alloys) such as AlSi10Mg and AlSi12 are widely used in various industries due to their high specific strength, excellent

processability, and low cost (Ref 9, 10). The Al–Si alloys have been extensively used to fabricate components for elevated temperature applications, such as automotive engine blocks, due to their excellent mechanical properties at elevated temperatures (Ref 11). The high temperature mechanical properties of additively manufactured samples can help to identify and design components for elevated temperatures. However, studies on the high-temperature mechanical properties of additively manufactured materials are very scarce in the literature, and the hot compression behavior of the additively manufactured AlSi10Mg alloy has not been reported so far. Furthermore, the high temperature performance of the additive sample can also be utilized to optimize the post-processing techniques based on hot working for additive manufacturing.

The hot working processes are one of the most prominent post-processing routes for additively manufactured alloys (Ref 12). The hot working of additively manufactured samples leads to improvement in the mechanical properties and reduction in the inherent defects present in the additive sample, such as porosity and lack of fusion (LOF). (Ref 13–15). These post-processing techniques are unsuitable for applications involving highly complex geometry, such as topology-optimized samples and internal lattice structures. The hot working process can improve the additive sample's mechanical properties, leading to a lighter design. Several deformation-based post-processing techniques have been explored by researchers for additively manufactured Al–Si alloys. P. Snopiński et al. (Ref 16) have investigated the effects of high temperature equi-channel angular pressing (ECAP) on additively manufactured Al–Si10Mg and observed increased strength and ductility. Similarly, Ali Hosseinzadeh et al. (Ref 17) have investigated the effect of the combination of multi-pass equal channel angular extrusion/pressing (ECAP) and selective laser melting on

Saurabh Gairola and R. Jayaganthan, Department of Engineering Design, Additive Manufacturing Group, and Center of Excellence for Materials and Manufacturing for Futuristic Mobility, Indian Institute of Technology Madras, Chennai 600036, India; and Gaurav Singh, Department of Engineering Design, Additive Manufacturing Group, and Center of Excellence for Materials and Manufacturing for Futuristic Mobility, Indian Institute of Technology Madras, Chennai 600036, India; and Department of Mechanical, Aerospace, and Nuclear Engineering, Rensselaer Polytechnic Institute, Troy, USA. Contact e-mail: edjay@iitm.ac.in.

AlSi12 alloy and observed an increase of 11% in ultimate tensile strength (UTS) and 55% in ductility after four passes of ECAP. The processing parameters of additively manufactured metals for hybrid or post-processing techniques can be optimized using high temperature flow behavior.

The flow stress behavior of the additively manufactured Al-Si alloys can be predicted using different constitutive models. Several models have been developed for predicting the dependence/sensitivity of flow stress on the strain, strain rate, and temperature, such as the Johnson–Cook model (Ref 18, 19), modified Johnson–Cook (Ref 20), strain-compensated Arrhenius equation (Ref 21–23), Zerilli–Armstrong model (Ref 24), Fields–Backofen model (Ref 25), and artificial neural network (ANN) (Ref 26–28). The constitutive models for predicting the flow stress behavior of the materials are broadly classified into three types: (a) phenomenological model, (b) physics-based models, and (c) ANN (Ref 29, 30). The physics-based model usually offers better predictive capability compared to the phenomenological model. The phenomenological model uses a much lower number of coefficients and is easier to implement than the physics-based models. Various studies have been performed on cast alloys to use these models and predict the strain rate, strain, and temperature-dependent high deformation behavior. The JC model and modified JC models have been used to predict the hot deformation behavior of additively manufactured Ti-6Al-4V (Ref 31, 32). The hot deformation behavior of additively manufactured FeCr alloy has been explored using the Johnson–Cook and modified Johnson–Cook models. The strain-compensated Arrhenius equation has been used to accurately predict the flow stress behavior in several alloys such as 17-4 PH steel, hot-rolled eutectoid steel, and extruded Mg-10Li-1Zn alloy (Ref 33–35). Similarly, the ANN model has been used to predict additively manufactured titanium alloys. The training of the network to accurately predict untested data requires a substantial amount of data (Ref 13), (Ref 31). Several other models are also being utilized to predict the flow stress behavior in the additively manufactured alloy, such as the Fields–Backofen model used to study the hot deformation behavior of Ti6Al4V alloy fabricated by a directed energy deposition (Ref 32). Considering that the deformation behaviors of additively manufacturing AlSi10Mg alloys are different from that of traditional alloys due to unique microstructure and the potential lightweight applications of AlSi10Mg alloy. The high temperature performance of the additively manufactured AlSi10Mg needs to be studied in detail.

However, studies on the deformation behavior and constitutive modeling of additive manufacturing AlSi10Mg alloy at elevated temperatures are very scarce in the literature.

The current research is focused on examining the hot deformation behavior of the additively manufactured AlSi10Mg alloy using isothermal hot compression testing using a Gleeble 3500 thermomechanical simulator. The experimental data were utilized to evaluate different constitutive models for predicting the flow stress in intermediate strain rates and temperatures. The results obtained were examined and compared using different statistical parameters, such as the coefficient of correlation (R), absolute average relative error (AARE) and root mean square error (RMSE), to provide an insight into the flow behavior of AlSi10Mg alloy fabricated using additive manufacturing route.

2. Experimental Procedure

The AlSi10Mg samples were printed using an “EOS M280 DMLS machine.” The samples were printed in the vertical orientation (as shown in Fig. 1a) using a meander scanning strategy, where the scan direction is rotated by 67° after each pass, as depicted in Fig. 1(b). The parameters used for the current study are shown in Table 1. The cylindrical samples of $12 \text{ mm} \times 8 \text{ mm}$ (ϕ) were machined from the additively manufactured sample as per ASTM E209 (Ref 36). The isostatic hot compression test was performed on the “Gleeble 3500 thermo-mechanical simulator.” The test was performed at four different temperatures (150, 200, 250, and 300 °C) and three different strain rates (0.01, 0.1, 1 s^{-1}).

The predictive capability/accuracy of different phenomenological models and artificial neural network (ANN) was evaluated and compared using different statistical parameters such as coefficient of correlation (R), average absolute relative error (AARE), and root mean square error (RMSE). These parameters are described using the following equation (Ref 37):

$$\text{AARE} = \frac{1}{N} \sum_{i=1}^N \left| \frac{\sigma_p - \sigma_{\text{exp}}}{\sigma_{\text{exp}}} \right| \times 100 \quad (\text{Eq 1})$$

$$\text{RMSE} = \sqrt{\frac{1}{N} \sum_{i=1}^n (\sigma_p - \sigma_{\text{exp}})^2} \quad (\text{Eq 2})$$

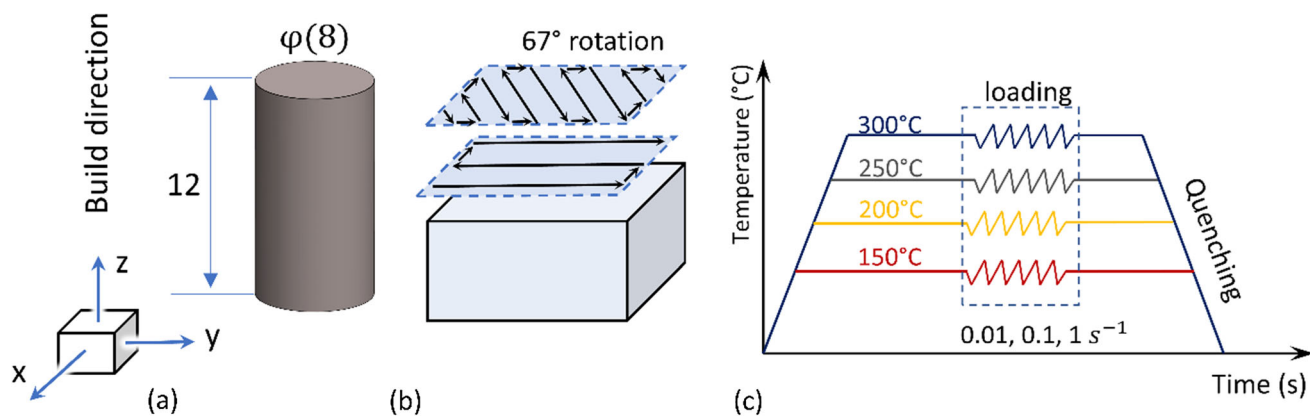


Fig. 1 (a) Specification of compression sample (all units are in mm), (b) Scanning strategy used for printing, (c) Procedure for hot compression

Table 1 Process parameter used for printing

Laser power, W	Scan speed, mm/s	Hatch spacing, mm	Layer thickness, μm	Preheat temperature, $^{\circ}\text{C}$
370	1300	0.19	30	300

Table 2 List of abbreviations used in the current study

Abbreviation	Full form
ANN	Artificial neural network.
AARE	Average absolute relative error.
RMSE	Root mean square error.
LPBF	Laser powder bed fusion.
AM	Additive manufacturing.
LOF	Lack of fusion.
ECAP	Equal channel angular pressing.
UTS	Ultimate tensile strength.
JC	Johnson–Cook model.
m-JC	Modified Johnson–Cook model.
SCAE	Strain-compensated Arrhenius equation.
ZA	Zerilli–Armstrong.
m-ZA	Modified Zerilli–Armstrong.
m-FB	Modified field Backofen.
ROI	Region of interest.
FCC	Face-centered cubic.
BCC	Body-centered cubic.

$$R = \frac{\sum_{i=1}^{i=N} (\sigma_{\text{exp}}^i - \bar{\sigma}_{\text{exp}}) (\sigma_p^i - \bar{\sigma}_p)}{\sqrt{\sum_{i=1}^{i=N} (\sigma_{\text{exp}}^i - \bar{\sigma}_{\text{exp}})^2 \sum_{i=1}^{i=N} (\sigma_p^i - \bar{\sigma}_p)^2}} \quad (\text{Eq 3})$$

$\bar{\sigma}_{\text{exp}}$ and $\bar{\sigma}_p$ are the mean value of σ_{exp} (experimental flow stress) and σ_p (flow stress predicted by different models), respectively. These parameters are calculated through a term-by-term comparison of predicted and experimental stress. The abbreviations used in the current study are shown in Table 2.

3. Results and Discussion

The flow stress behavior of additively manufactured alloy in different strain rates and temperatures is shown in Fig. 2. The flow stress increases linearly in the initial region with an increase in the strain, followed by softening, leading to a decrease in the flow stress. The effect of deformation conditions on flow stress can be observed using peak stress under different deformation conditions. The distribution of the peak stress is shown in Table 3. The peak stress increases with an increase in strain rate and a decrease in temperature. The stress–strain data from the uniaxial compressive test can be used to determine the material constants of different constitutive models. These constitutive models can be used to determine the flow stress for intermediate deformation conditions (strain rate and temperature). Different phenomenological models and artificial neural network (ANN) were employed to analyze and predict the flow stress behavior of the additively manufactured

AlSi10Mg: (a) the Johnson–Cook (JC) model, (b) modified Johnson–Cook (m-JC) model, (c) strain-compensated Arrhenius equation (SCAE), (d) modified Fields–Backofen (m-FB) model, and (e) modified Zerilli–Armstrong (m-ZA) model.

3.1 Initial Microstructure

Figure 3 shows the initial microstructure of the additively manufactured AlSi10Mg alloy. The microstructure of the as-built sample shows a fine cellular structure with a cell size of 597 ± 145 nm. The cell size was evaluated using the line intercept method using “ImageJ software.” The zoomed image of the region of interest (ROI) of Fig. 3(a) is shown in Fig. 3(b). The Mg-rich precipitates (Mg_2Si) were observed at the edge of the cellular network. The detailed characterization of the precipitates is discussed in our previous studies (Ref 6, 38). These precipitates can have a stabilizing effect on microstructural features at elevated temperatures. The precipitates or second phase particles pin the grain boundaries at elevated temperatures and restrict grain growth by the Zener pinning phenomenon. The combined effect of the small grain size of the additively manufactured sample and the pinning effect of precipitates might be responsible for the high peak strength at elevated temperatures, as shown in Table 3.

3.2 Johnson–Cook Model (JC)

The Johnson–Cook model is one of the oldest and most widely used phenomenological models used for predicting the flow stress/plastic stress of material under a variety of temperatures and strain rates. The original Johnson–Cook model is shown in Eq. 4 (Ref 39).

$$\sigma = [A + B\varepsilon^n] \left[1 + C \ln \left(\frac{\dot{\varepsilon}}{\dot{\varepsilon}_0} \right) \right] \left[1 - \left(\frac{T - T_{\text{ref}}}{T_{\text{melt}} - T_{\text{ref}}} \right)^m \right] \quad (\text{Eq 4})$$

Here, A , B , C , n , and m are material constants, and σ and ε are flow stress and the corresponding plastic strain. $\dot{\varepsilon}_0$ is the reference strain rate, and T_{ref} , T_{melt} are reference and melting temperatures (873 K (Ref 40)), respectively. The Johnson–Cook model consists of elements correlating the flow stress with strain hardening, strain rate hardening, and thermal softening in the material. The form of the Johnson–Cook model (JC consists of three independent terms in multiplication) suggests that these three effects are independent. Hence, the JC model can give an accurate prediction for the materials where the interdependency of strain rate and temperature is minimal.

In the current study, the reference temperature and strain rate were chosen as 423 K (150 $^{\circ}\text{C}$) and 0.01 s^{-1} , respectively. The procedure for determining the Johnson–Cook parameters is described below. At reference strain rate and reference temperature, the JC equation reduces to:

$$\sigma = A + B\varepsilon^n \text{ or } \sigma - A = B\varepsilon^n \quad (\text{Eq 5})$$

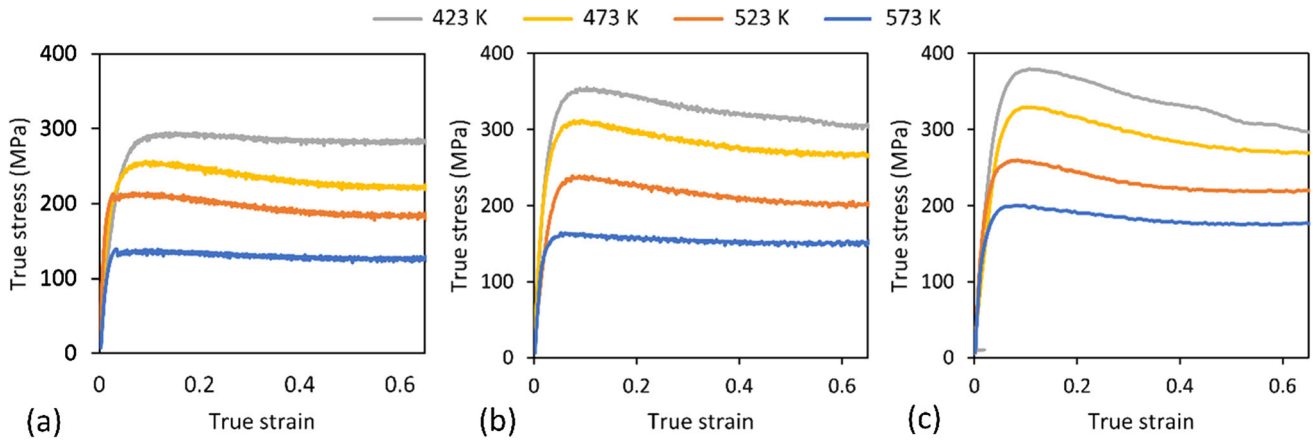


Fig. 2 Flow stress behavior at different temperatures for a strain rate of 0.01 s⁻¹, (b) 0.1 s⁻¹, (c) 1 s⁻¹

Table 3 Peak stress for different strain rates and temperatures

	Temperature, °C	Strain rate, s ⁻¹		
		0.01, MPa	0.1, MPa	1, MPa
	150 °C	295	355	380
	200 °C	256	312	330
	250 °C	215	239	260
	300 °C	139	164	200

Here 'A' is the 0.2% yield strength at the reference temperature and reference strain rate. Taking natural logarithms on both sides

$$\ln(\sigma - A) = \ln B + n \ln \epsilon \quad (\text{Eq 6})$$

The slope of the linear regression between $\ln(\sigma - A)$ and $\ln \epsilon$ gives material constant n, and the y-intercept gives $\ln B$. The constants B and n are evaluated as 69.4 MPa and 0.0463, respectively.

At reference temperature,

$$\sigma = (A + B\epsilon^n) \left(1 + C \ln \left(\frac{\dot{\epsilon}}{\dot{\epsilon}_0} \right) \right)$$

$$\frac{\sigma}{(A + B\epsilon^n)} = \left(1 + C \ln \left(\frac{\dot{\epsilon}}{\dot{\epsilon}_0} \right) \right) \quad (\text{Eq 7})$$

The relationship between $\frac{\sigma}{(A + B\epsilon^n)}$ and $\ln \left(\frac{\dot{\epsilon}}{\dot{\epsilon}_0} \right)$ is shown in Fig. 4(a). The slope of linear regression with a y-intercept of 1 gives us the constant C.

Similarly, at the reference strain rate,

$$\sigma = [A + B\epsilon^n] \left[1 - \left(\frac{T - T_{\text{ref}}}{T_{\text{melt}} - T_{\text{ref}}} \right)^m \right] \text{ or } 1 - \frac{\sigma}{[A + B\epsilon^n]}$$

$$= \left(\frac{T - T_{\text{ref}}}{T_{\text{melt}} - T_{\text{ref}}} \right)^m \quad (\text{Eq 8})$$

Taking natural logarithms on both sides:

$$\ln \left(1 - \frac{\sigma}{[A + B\epsilon^n]} \right) = m \cdot \ln \left(\frac{T - T_{\text{ref}}}{T_{\text{melt}} - T_{\text{ref}}} \right) \quad (\text{Eq 9})$$

The relationship between $\ln \left(1 - \frac{\sigma}{[A + B\epsilon^n]} \right)$ and $\ln \left(\frac{T - T_{\text{ref}}}{T_{\text{melt}} - T_{\text{ref}}} \right)$ is shown in Fig. 4(b). The slope of the linear regression with a y-intercept of 0 gives us the constant 'm.' The constants for the Johnson–Cook model are summarized in Table 4.

The comparison between the experimental and predicted flow stress of the selective laser-melted AlSi10Mg under different stress rates and temperatures is shown in Fig. 5. It can be observed that the predictive capability of the Johnson–Cook model on the flow stress of AlSi10Mg alloy in the current study is low.

3.3 Modified Johnson–Cook Model (m-JC)

The original JC model assumes that the thermal softening of the material is independent of the strain rate and strain hardening effect. However, it can be observed from flow stress behavior in the current study that the thermal softening changes with the strain rate. This coupling effect of strain rate on thermal softening was included in the modified JC model as follows: (Ref 41, 42)

$$\sigma = (A_1 + B_1\epsilon + B_2\epsilon^2) \left[1 + C_1 \ln \left(\frac{\dot{\epsilon}}{\dot{\epsilon}_0} \right) \right]$$

$$\exp \left[\left(\lambda_1 + \lambda_2 \ln \left(\frac{\dot{\epsilon}}{\dot{\epsilon}_0} \right) \right) (T - T_{\text{ref}}) \right] \quad (\text{Eq 10})$$

At the reference strain rate (0.01 s⁻¹) and reference temperature (150 °C)

$$\sigma = (A_1 + B_1\epsilon + B_2\epsilon^2) \quad (\text{Eq 11})$$

Second-order polynomial regression was used for the plot between σ and ϵ as depicted in Fig. 6(a), and the coefficient of the polynomial regression gives constants A_1 , B_1 , and B_2 . The values of constants A_1 , B_1 , and B_2 are obtained as 276.3, 150.7, and -270 MPa, respectively.

At reference temperature,

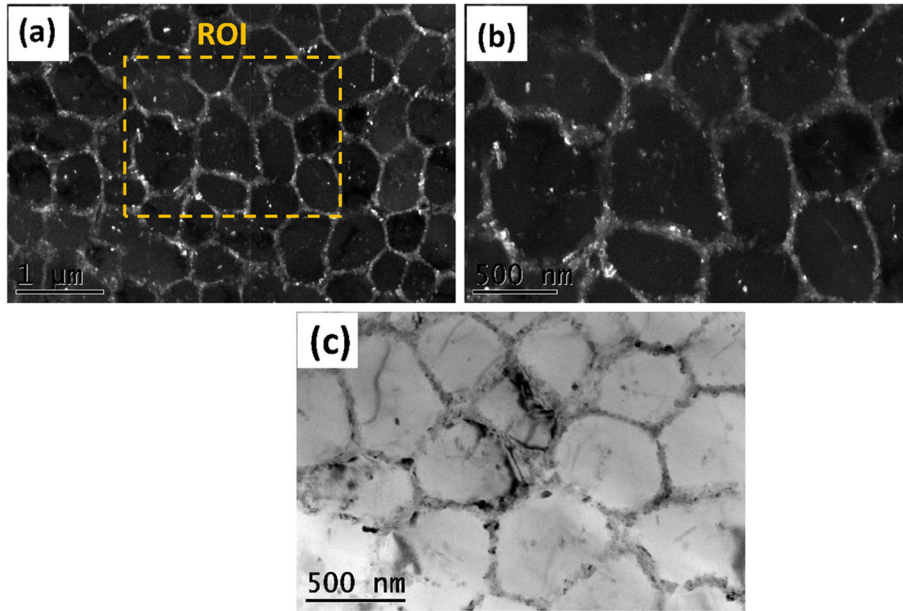


Fig. 3 Initial microstructure using dark field image with region of interest (ROI), (b) dark field of ROI and (c) bright field image

Table 4 Coefficient of Johnson–Cook model

	<i>A</i> , MPa	<i>B</i> , MPa	<i>C</i>	<i>n</i>	<i>m</i>
Value	227.8	69.4	0.0463	0.153	0.801

$$\sigma = (A_1 + B_1\epsilon + B_2\epsilon^2) \left[1 + C_1 \ln\left(\frac{\dot{\epsilon}}{\dot{\epsilon}_0}\right) \right] \quad (\text{Eq 12})$$

$$\frac{\sigma}{(A_1 + B_1\epsilon + B_2\epsilon^2)} = \left[1 + C_1 \ln\left(\frac{\dot{\epsilon}}{\dot{\epsilon}_0}\right) \right]$$

The linear regression between $\frac{\sigma}{(A_1 + B_1\epsilon + B_2\epsilon^2)}$ and $\ln\left(\frac{\dot{\epsilon}}{\dot{\epsilon}_0}\right)$ with a y-intercept of 1 was plotted for different strain rates (0.01 s⁻¹, 0.1 s⁻¹ and 1 s⁻¹), and the slope of the linear regression gives constant *C*₁. The average slope of the linear fitting curve (*C*₁) is 0.049.

$$\frac{\sigma}{(A_1 + B_1\epsilon + B_2\epsilon^2) \left[1 + C_1 \ln\left(\frac{\dot{\epsilon}}{\dot{\epsilon}_0}\right) \right]} = \exp \left[\left(\lambda_1 + \lambda_2 \ln\left(\frac{\dot{\epsilon}}{\dot{\epsilon}_0}\right) \right) (T - T_{\text{ref}}) \right] \quad (\text{Eq 13})$$

Taking logarithms on both sides,

$$\ln \left(\frac{\sigma}{(A_1 + B_1\epsilon + B_2\epsilon^2) \left[1 + C_1 \ln\left(\frac{\dot{\epsilon}}{\dot{\epsilon}_0}\right) \right]} \right) = \left(\lambda_1 + \lambda_2 \ln\left(\frac{\dot{\epsilon}}{\dot{\epsilon}_0}\right) \right) (T - T_{\text{ref}}) \quad (\text{Eq 14})$$

The coefficients obtained for the modified Johnson–Cook model are shown in Table 5. The modified Johnson–Cook model shows better accuracy compared to the original Johnson–Cook model. This higher accuracy might be accredited to the incorporation of the coupling effect of strain rate and

temperature in the modified Johnson–Cook model. Figure 7 depicts the comparison of experimental and predicted stress–strain curves using a modified JC model. The modified Johnson–Cook model shows a better fit compared to the original JC model.

3.4 Strain-Compensated Arrhenius Equation (SCAE)

Arrhenius model is the most widely used model for predicting the flow behavior of material for high stress. The Arrhenius model defines the correlation of flow behavior with strain rate and temperature, using different equations for different ranges of stress. According to the Arrhenius model, the relationship between flow stress, temperature, and strain rate can be defined using power law for low-stress range, exponential law for high-stress level, and hyperbolic sine function for all stress, as shown in Eq. 15 and 16 (Ref 43).

$$\dot{\epsilon} = A \cdot F(\sigma) \cdot \exp\left(-\frac{Q}{RT}\right) \quad (\text{Eq 15})$$

where

$$F(\sigma) = \begin{cases} \sigma^{n_1}, & \sigma\alpha < 0.8 \\ \exp(\beta\sigma) & \sigma\alpha > 1.2 \\ \{\sinh(\alpha n)\}^n & \text{for all } \sigma \end{cases} \quad (\text{Eq 16})$$

Here 'Q' is the activation energy (kJmol⁻¹), and R is the universal gas constant (8.314 J mol⁻¹ K⁻¹). $\dot{\epsilon}$ is strain rate (s⁻¹), σ is flow stress (MPa), and T is the absolute temperature (K). *A*, *n*₁, β , *n*, and α are material constants.

Taking natural logarithms on both sides:

$$\ln \dot{\epsilon} = \begin{cases} \ln A_1 + n_1 \ln \sigma - \frac{Q}{RT}, & \text{for } \sigma\alpha < 0.8 \\ \ln A_2 + \beta\sigma - \frac{Q}{RT}, & \text{for } \sigma\alpha > 1.2 \\ n A_1 + n \ln(\sinh(\alpha\sigma)) - \frac{Q}{RT}, & \text{for all } \sigma \end{cases} \quad (\text{Eq 17})$$

The slope of the plot between $\ln \dot{\epsilon}$ and $\ln \sigma$ gives us constant *n*₁, whereas the slope of the plot between $\ln \dot{\epsilon}$ and σ gives us constant β as shown in Fig. 8. The ratio of β to *n*₁ is constant α .

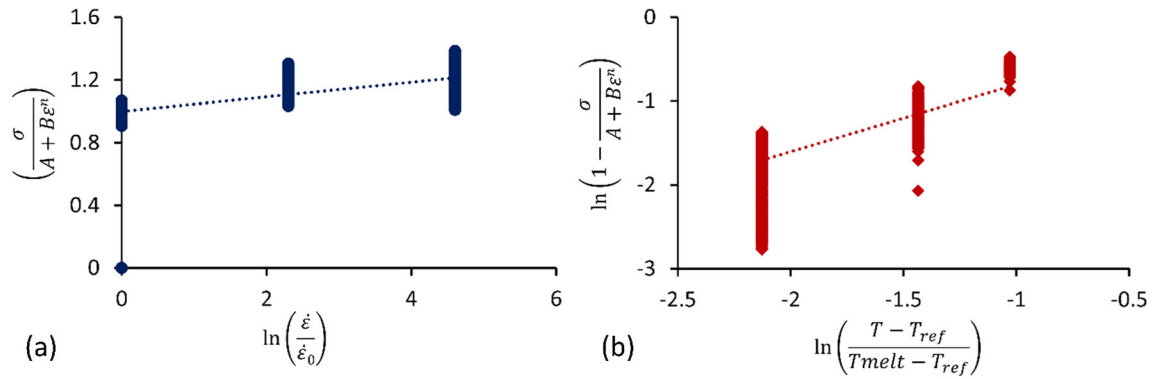


Fig. 4 Parameter calculation for the Johnson–Cook model

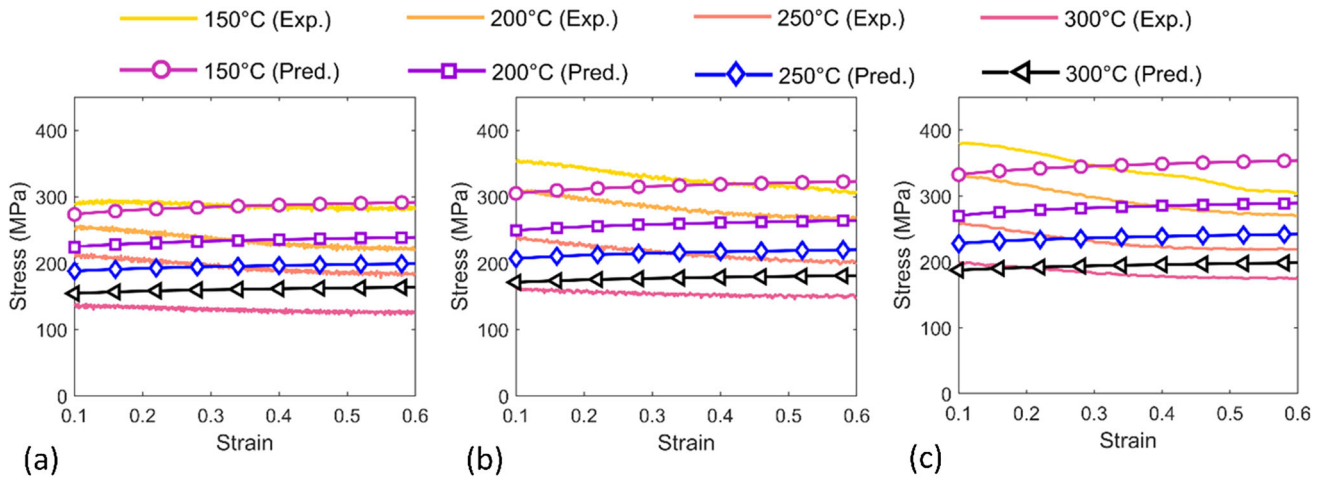


Fig. 5 Comparison between experimental and predicted stress–strain curves by Johnson–Cook model (a) 0.01 s^{-1} , (b) 0.1 s^{-1} , (c) 1 s^{-1}

Table 5 Modified Johnson–Cook model constants

	A_1 , MPa	B_1 , MPa	B_2 , MPa	C_1	λ_1	λ_2
Value	276.3	150.7	−270	0.049	−0.00504	0.000123

These constants were evaluated for each strain, ranging from 0.06 to 0.6.

$$n_1 = \frac{\partial \ln \dot{\epsilon}}{\partial \ln \sigma}, \beta = \frac{\partial \ln \dot{\epsilon}}{\partial \sigma}, \text{ and } \alpha = \frac{\beta}{n_1} \quad (\text{Eq 18})$$

Similarly, the activation energy is evaluated from the slope of the linear regression between $(1/T)$ and $\ln[\sinh(\alpha\sigma)]$ using the following equation:

$$Q = R \left(\frac{\partial \ln \dot{\epsilon}}{\partial \ln[\sinh(\alpha\sigma)]} \right) \left(\frac{\partial \ln[\sinh(\alpha\sigma)]}{\partial (1/T)} \right) \quad (\text{Eq 19})$$

The constant n , A is evaluated using the Zener–Hollomon parameter evaluated using the following equation:

$$Z = \dot{\epsilon} \exp\left(\frac{Q}{RT}\right) = A[\sinh(\alpha\sigma)]^n \quad (\text{Eq 20})$$

$$\ln Z = \ln A + n \ln \sinh(\alpha\sigma) \quad (\text{Eq 21})$$

The slope of linear regression between $\ln Z$ and $\ln \sinh(\alpha\sigma)$ gives us constant n , and the y-intercept gives the constant $\ln A$.

The original Arrhenius equation does not consider the effect of the strain on the prediction of flow stress. The effect of strain, such as strain hardening, is a significant component of the flow stress, and hence, the strain-compensated Arrhenius equation (SCAE) was used. The material constants of the Arrhenius equation were assumed to be a polynomial function of the strain. The material constants were calculated for ten incremental strain values. This approach of defining the material constant in terms of strain is unique compared to the other models, which have a constant value of coefficients. The order of the polynomial was varied from 3 to 6, and the minimum error value was chosen as the final value. The AARE for 3rd, 4th, 5th, and 6th order polynomials is 4.2, 5.4, 4.1, and

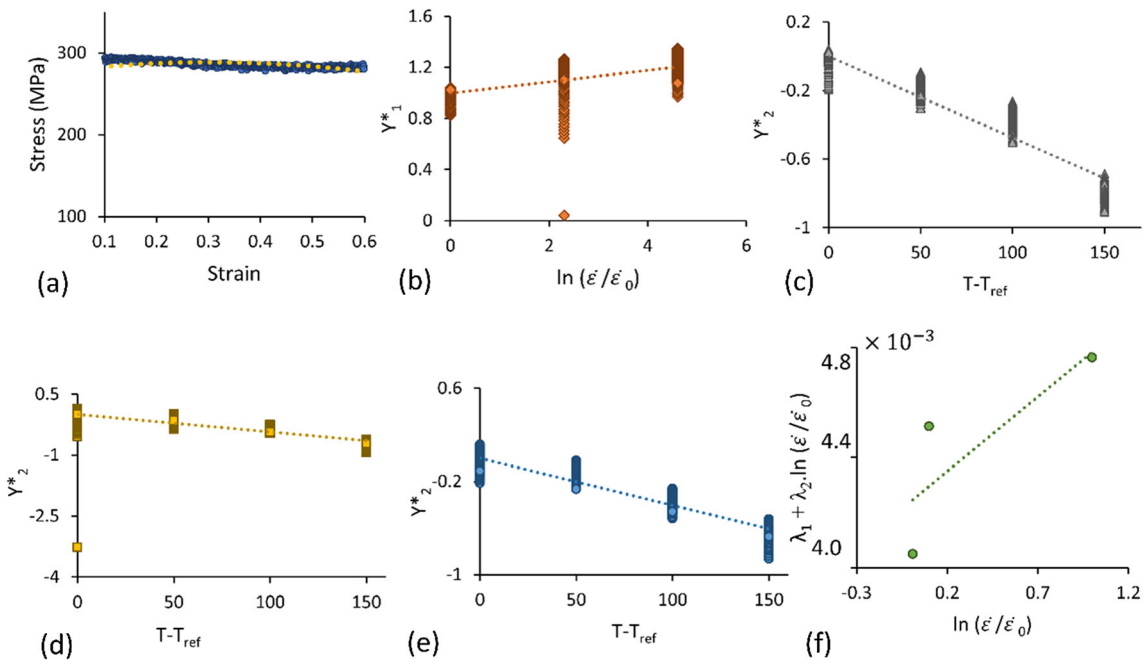


Fig. 6 (a) Second-order polynomial regression at reference temperature and reference strain rate (b) $Y_1^* = \frac{\sigma}{(A_1 + B_1\epsilon + B_2\epsilon^2)}$ versus $\ln\left(\frac{\dot{\epsilon}}{\dot{\epsilon}_0}\right)$ relation curve, $Y_2^* = \ln\left(\frac{\sigma}{(A_1 + B_1\epsilon + B_2\epsilon^2)} \left[1 + C_1 \ln\left(\frac{\dot{\epsilon}}{\dot{\epsilon}_0}\right)\right]\right)$ versus $T - T_{ref}$ for three strain rates of (c) 0.01 s^{-1} (d) 0.1 s^{-1} (e) 1 s^{-1} , and (f) $\lambda_1 + \lambda_2 \ln\left(\frac{\dot{\epsilon}}{\dot{\epsilon}_0}\right)$ versus $\ln\left(\frac{\dot{\epsilon}}{\dot{\epsilon}_0}\right)$ plot

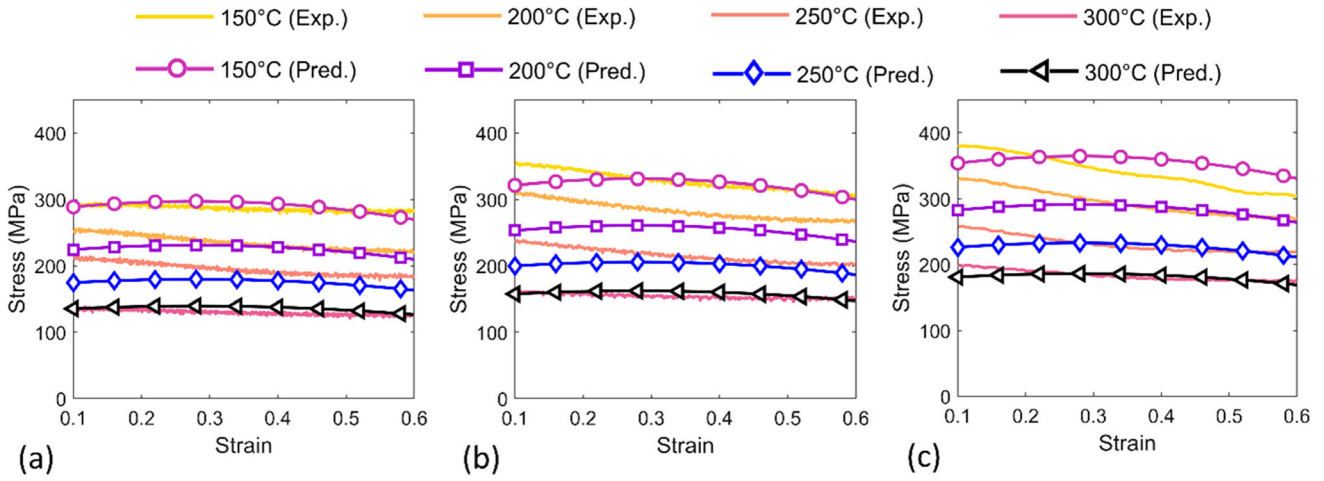


Fig. 7 Comparison between experimental and predicted stress–strain curves by modified Johnson–Cook model (a) 0.01 s^{-1} , (b) 0.1 s^{-1} , (c) 1 s^{-1}

6.1, respectively. Hence, the 5th-order polynomial with a minimum AARE value was chosen, and the polynomial fit with the corresponding R^2 is shown in Fig. 9. The coefficients for the sixth-order polynomial fit of the material are listed in Table 6.

$$\alpha = A_0 + A_1\epsilon + A_2\epsilon^2 + A_3\epsilon^3 + A_4\epsilon^4 + A_5\epsilon^5$$

$$n = B_0 + B_1\epsilon + B_2\epsilon^2 + B_3\epsilon^3 + B_4\epsilon^4 + B_5\epsilon^5$$

$$Q = C_0 + C_1\epsilon + C_2\epsilon^2 + C_3\epsilon^3 + C_4\epsilon^4 + C_5\epsilon^5$$

$$\ln A = D_0 + D_1\epsilon + D_2\epsilon^2 + D_3\epsilon^3 + D_4\epsilon^4 + D_5\epsilon^5 \quad (\text{Eq 22})$$

The Zener–Hollomon parameter can be defined using Eq. 20.

The flow stress using the Arrhenius equation can be defined by Eq.23

$$\sigma = \frac{1}{\alpha} \left[\left(\frac{Z}{A} \right)^{1/n} + \left\{ 1 + \left(\frac{Z}{A} \right)^{2/n} \right\}^{1/2} \right] \quad (\text{Eq 23})$$

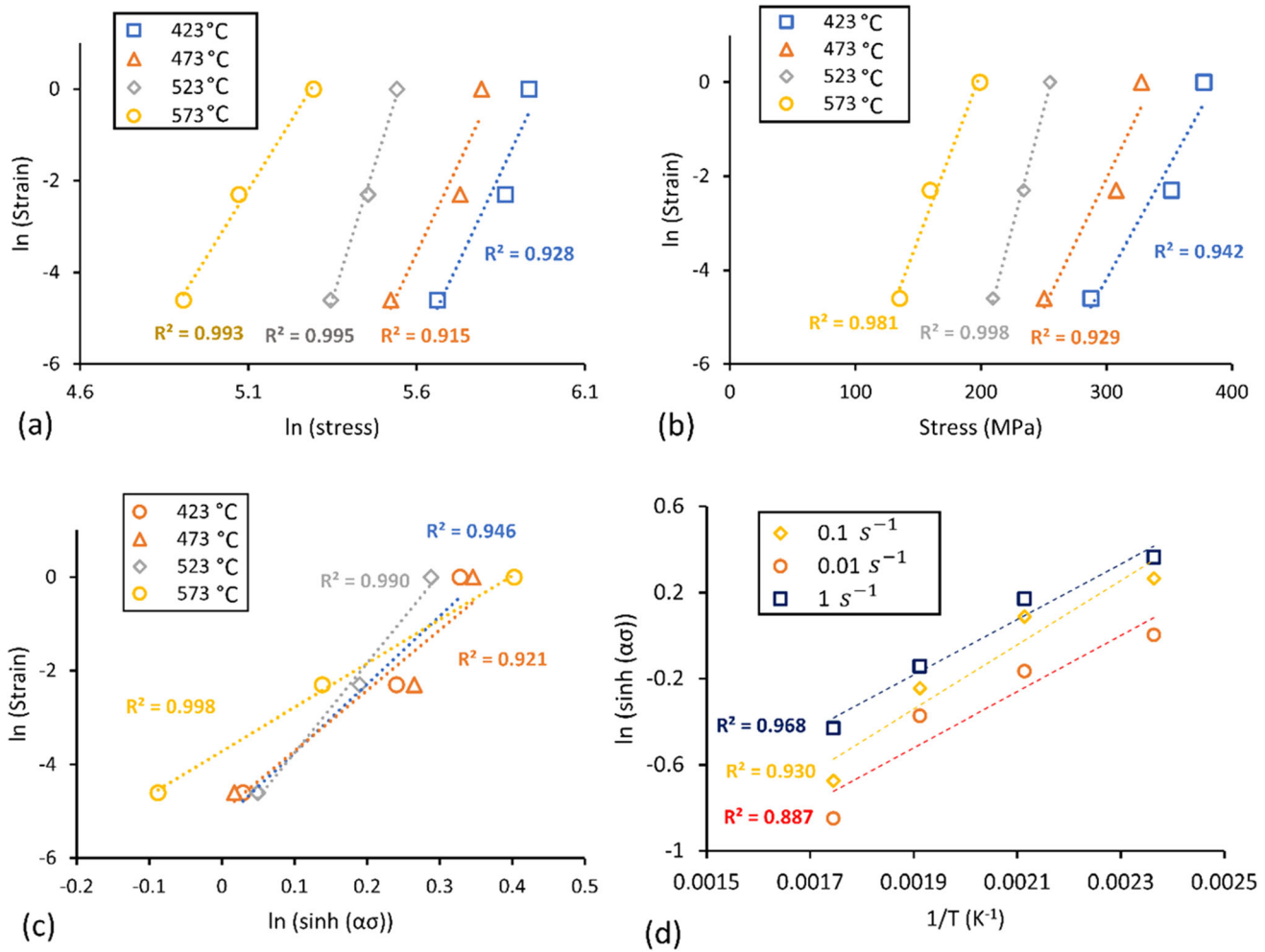


Fig. 8 Parameter calculation for SCAE

Table 6 Parameter for strain-compensated Arrhenius equation

Q, kJMol^{-1}	α, MPa^{-1}	n	$\ln(A)$
$A_0 = 210.1$	$B_0 = 0.043$	$C_0 = 11.45$	$D_0 = 27.47$
$A_1 = -214.72$	$B_1 = -0.331$	$C_1 = -187.1$	$D_1 = 4.075$
$A_2 = 1203.7$	$B_2 = 1.244$	$C_2 = 1537.3$	$D_2 = 178.14$
$A_3 = -2622.1$	$B_3 = -2.382$	$C_3 = -4680.5$	$D_3 = -515.76$
$A_4 = 2187.25$	$B_4 = 2.43$	$C_4 = 6113.8$	$D_4 = 384.94$
$A_5 = -267.3$	$B_5 = -1.027$	$C_5 = -2901.4$	$D_5 = -16.98$

Figure 10 shows the comparison between experimental and predicted flow stress behavior using the Arrhenius equation. The flow stress predicted using the Arrhenius equation shows a larger error at low strain, but the overall prediction is in good agreement with the experimental observation.

3.5 Modified Fields–Backofen (m-FB) Model

The original Fields–Backofen equation describes the relationship of flow stress with strain and strain rate as $\sigma = k\epsilon^n \dot{\epsilon}^m$, where k is the stress coefficient, n is the strain hardening exponent, and m is the strain rate sensitivity index. This equation has been modified to extend its modeling ability for

thermal softening at elevated temperatures. This modified equation can be expressed as (Ref 44)

$$\sigma = k\epsilon^n \dot{\epsilon}^m \exp(bT + s\epsilon) \quad (\text{Eq 24})$$

b is the material constant, and s is the softening ratio. Taking logarithms on both sides of the equation:

$$\ln\sigma = \ln k + n\ln\epsilon + m\ln\dot{\epsilon} + bT + s\epsilon \quad (\text{Eq 25})$$

The parameters n , m , and b were calculated using the slope of the linear regression between $\ln\sigma - \ln\epsilon$, $\ln\sigma - \ln\dot{\epsilon}$, and $\ln\sigma - T$, respectively.

$$n = \frac{\partial \ln\sigma}{\partial \ln\epsilon}, \quad m = \frac{\partial \ln\sigma}{\partial \ln\dot{\epsilon}}, \quad \text{and} \quad b = \frac{\partial \ln\sigma}{\partial T} \quad (\text{Eq 26})$$

The constants of the equation were correlated with the deformation temperature and strain rate as follows:

$$k = k_1 + K_2 \ln\dot{\epsilon} + K_3/T$$

$$n = n_1 + n_2 \ln\dot{\epsilon} + n_3/T \quad (\text{Eq 27})$$

$$m = m_1 + m_2/T$$

The variation of constant n , with different strain rates and temperatures, is shown in Fig. 11(a). The constants

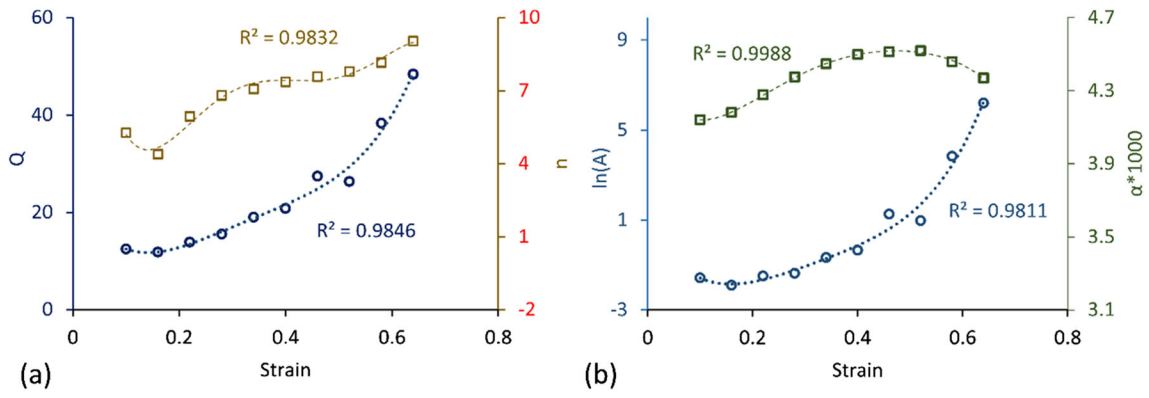


Fig. 9 Sixth-order polynomial fit for Q , n , $\ln(A)$, and α

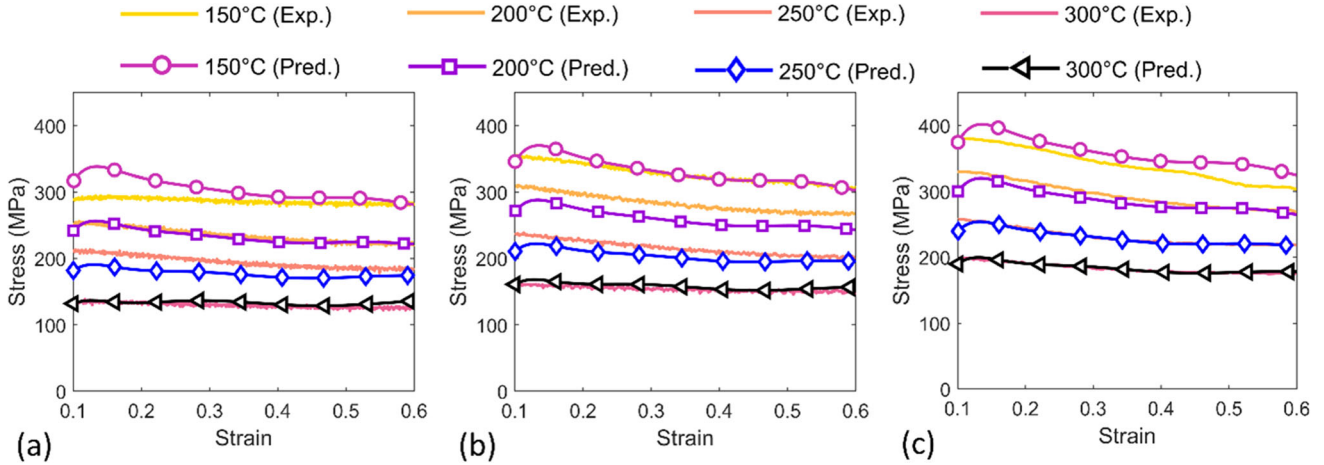


Fig.10 Comparison between experimental and predicted stress–strain curves by strain-compensated Arrhenius model (a) 0.01 s^{-1} , (b) 0.1 s^{-1} , (c) 1 s^{-1}

$n_1, n_2,$ and n_3 were obtained from the regression method. Similarly, the constants $m_1,$ and m_2 were obtained by performing the linear regression between the parameter m and $(1/T)$, as shown in Fig. 11(c).

$$K_0 = \ln k + m \ln \dot{\epsilon} + bT, \text{ and hence } \ln \sigma = K_0 + n \ln \dot{\epsilon} + s \epsilon \quad (\text{Eq 28})$$

For $\epsilon = e^{-1}$, $\ln(\sigma_{e^{-1}}) = K_0 - n + s e^{-1}$ and for $\epsilon = e^{-2}$, $\ln(\sigma_{e^{-2}}) = K_0 - 2n + s e^{-2}$. Subtracting $\ln(\sigma_{e^{-2}})$ from $\ln(\sigma_{e^{-1}})$ we get:

$$s = \frac{1}{e^{-1} - e^{-2}} \times \left\{ \ln \left(\frac{\sigma_{e^{-1}}}{\sigma_{e^{-2}}} \right) - n \right\} \quad (\text{Eq 29})$$

The values of s at different temperatures and strain rates are calculated using experimental data. The coefficient for the m-FB model is shown in Table 7. Figure 12 shows the experimental and predicted flow stress–strain curve using modified Fields–Backofen model. The m-FB model shows excellent predictive capability for a wide range of deformation conditions (strain, strain rate, and temperature).

3.6 Modified Zerilli–Armstrong (m-ZA) Model

Zerilli–Armstrong (ZA) model is a semi-empirical model for predicting the flow stress in the material. ZA model is developed according to the dislocation mechanism prevalent

Table 7 Modified Field Backofen model parameter

	K_1	K_2	K_3	n_1	n_2
Value	42238.1	−1611	−13526860	0.048711	−0.0084
	n_3	m_1	m_2	b	s
Value	−22.4	0.132	0.000216	−0.00787	−0.330

in metallic materials during plastic deformation. As per ZA model, the flow model is divided into thermal and athermal components.

$$\sigma = \sigma_{th} + \sigma_a \quad (\text{Eq 30})$$

Here, σ_a and σ_{th} are the athermal activation and thermal activation flow stress, respectively. The unique characteristic of this model is that each material structure type has a different expression due to the different strain-controlling mechanisms. The thermal activation flow stress for FCC and BCC material is given as (Ref 45):

$$\sigma_{th} = \begin{cases} C_1 \dot{\epsilon}^n \{ \exp(-C_3 T + C_4 T \ln \dot{\epsilon}^*) \}, & \text{for bcc material} \\ C_0 + C_2 \{ e^{0.5(-C_3 T + C_4 T \ln \dot{\epsilon}^*)} \}, & \text{for fcc material} \end{cases} \quad (\text{Eq 31})$$

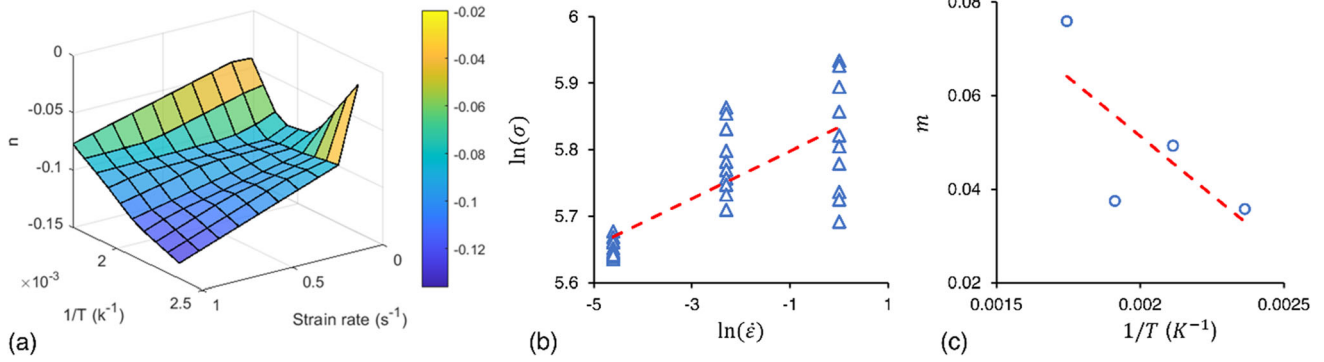


Fig. 11 (a) Variation of parameter n with different strain rates and temperature, (b) linear fit of $\ln\sigma - \ln\dot{\epsilon}$ curve, and (c) linear fit between parameter $m - (1/T)$ curve

An additional term C_0 is added to include the effect of athermal component and the effect of yield stress on grain size. Hence, the original Zerilli–Armstrong model for different types of metals can be expressed as:

$$\sigma = \begin{cases} C_0 + C_1 \dot{\epsilon}^n \{ \exp(-C_3 T + C_4 T \ln \dot{\epsilon}^*) \} + C_5 \dot{\epsilon}^n, & \text{for } bcc \text{ material} \\ C_0 + C_2 \{ e^{0.5(-C_3 T + C_4 T \ln \dot{\epsilon}^*)} \}, & \text{for } fcc \text{ material} \end{cases} \quad (\text{Eq 32})$$

The original Zerilli–Armstrong model considers the effect of the dislocation mechanism but fails to correlate the flow stress with the deformation condition (strain rate and temperature). This can severely limit the predictive capability of the original ZA model. Samantaray et al. (Ref 46) modified the ZA model to include the effect of thermal softening, strain rate hardening, and strain hardening. The modified Zerilli–Armstrong model is expressed as follows: (Ref 47)

$$\sigma = (C_1 + C_2 \dot{\epsilon}^n) \exp\{-(C_3 + C_4 \dot{\epsilon}) T^* + (C_5 + C_6 T^*) \ln \dot{\epsilon}^*\} \quad (\text{Eq 33})$$

$$T^* = T - T_{\text{ref}} \text{ and } \dot{\epsilon}^* = \dot{\epsilon} / \dot{\epsilon}_0$$

Here, C_1, C_2, C_3, C_5, C_6 , and n are material constants. Taking natural logarithm on both sides, the equation becomes:

$$\ln \sigma = \ln(C_1 + C_2 \dot{\epsilon}^n) - (C_3 + C_4 \dot{\epsilon}) T^* + (C_5 + C_6 T^*) \ln \dot{\epsilon}^* \quad (\text{Eq 34})$$

For reference strain rate (0.01 s^{-1}), equation (34) can be expressed as:

$$\ln \sigma = \ln(C_1 + C_2 \dot{\epsilon}^n) - (C_3 + C_4 \dot{\epsilon}) T^* \quad (\text{Eq 35})$$

The slope and y-intercept of the linear regression between $\ln \sigma - T^*$ is $S_1 = C_3 + C_4 \dot{\epsilon}$, and $Y_1 = \ln(C_1 + C_2 \dot{\epsilon}^n)$. An example of the linear fit between $\ln \sigma$ and T^* for the strain value of 0.1 is shown in Fig. 13(a). The equation for intercept Y_1 can be rearranged as:

$$\ln(\exp Y_1 - C_1) = \ln C_2 + n \ln \dot{\epsilon} \quad (\text{Eq 36})$$

The slope and y-intercept of the linear regression between S_1 and $\dot{\epsilon}$ give us constant C_3 and C_4 as shown in Fig. 13(b). Similarly, the slope and y-intercept of the linear regression between the $\ln(\exp Y_1 - C_1)$, and $\ln \dot{\epsilon}$ give us constant C_2 , and n as shown in Fig. 12(c). C_1 is the yield strength of the material

at reference strain rate (0.01 s^{-1}) and reference temperature ($150 \text{ }^\circ\text{C}$). The slope of the plot between $\ln \sigma$ and $\ln \dot{\epsilon}^*$ is $S_2 = (C_5 + C_6 T^*)$. The slope is plotted with T^* , the slope of the S_2 versus T^* gives us C_6 , and the y-intercept gives us C_5 . The parameters evaluated for m-ZA model are shown in Table 8. Figure 14 depicts the comparison between experimental stress and flow stress predicted using the m-ZA model. The m-ZA model shows excellent predictive capability at elevated temperatures. However, the prediction capability for intermediate temperature is poor.

3.7 Artificial Neural Network (ANN)

ANN or artificial neural networks are data-driven and nonlinear statistical models that can recognize and predict the complex relationship between the input and output data set. The ANN model consists of a processing unit called a neuron, and each neuron in the hidden layer represents one independent variable. The predicted flow stress was determined with the help of the feed-forward back propagation and Levenberg–Marquardt (L-M) training algorithm. The L-M algorithm is a very efficient algorithm for optimizing complex nonlinear problems. The back-propagation mechanism optimizes the solution by minimizing the RMSE (root mean square error) between experimental and predicted flow stress. The RMSE was chosen as an objective function instead of R^2 because the higher value of R^2 does not necessarily correspond to better performance of the model. R^2 can be biased toward the higher or lower end of the distribution (Ref 48). Hence, RMSE, which is an unbiased parameter, is preferred over R^2 as the objective function.

The schematic diagram of the ANN structure for flow stress prediction is shown in Fig. 15(a). The strain, temperature, and strain rate were taken as the input variable, whereas the flow stress was taken as the output variable. The input dataset was randomly divided into three datasets: a training dataset (used for fitting the model), a validation dataset (used for fine-tuning the parameter during training), and a test dataset (used for unbiased evaluation of the final model fit). The training, test, and validation set were set as the 75:15:10 portion of dataset. The input variable is combined to form a new, complex variable in the hidden layer. The number of optimal hidden neurons depends on the nature and complexity of the optimization problem. The number of neurons in the hidden layer of a neural

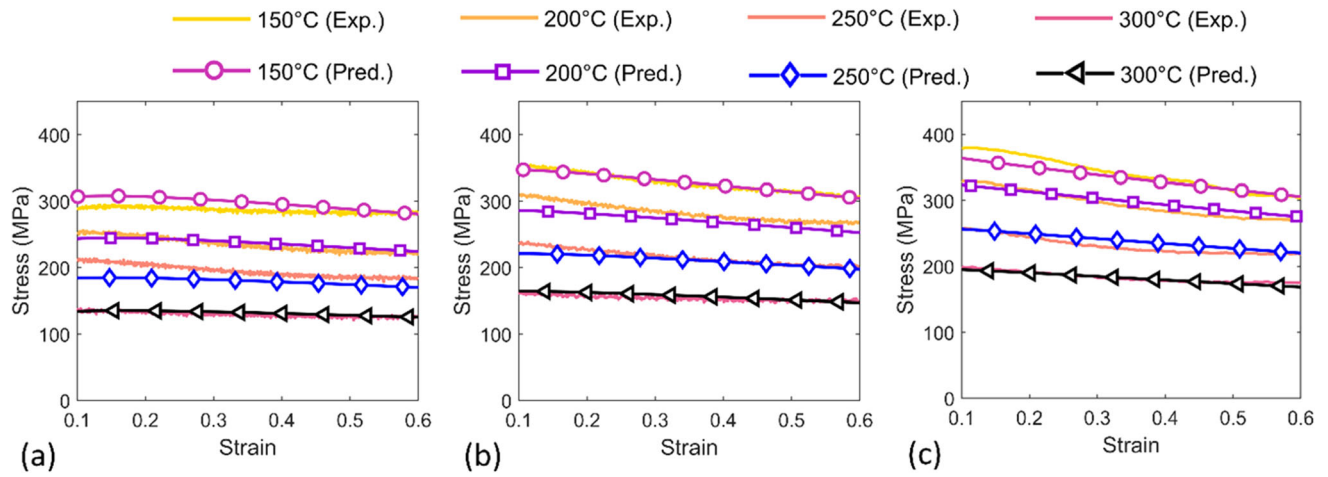


Fig. 12 Comparison between experimental and predicted stress–strain curves by modified Fields–Backofen model (a) 0.01 s^{-1} , (b) 0.1 s^{-1} , (c) 1 s^{-1}

Table 8 Parameter for modified Zerilli–Armstrong model

	C_1 , MPa	C_2 , MPa	C_3	C_4	C_5	C_6	n
Value	227.8	62.65	0.0052	0.000728	0.0341	0.000244	−0.110

network can greatly affect the predictive capability of the ANN model. If the number of neurons is very low (the architecture is too simple), the resulting ANN network will not have sufficient capability for accurate prediction. On the other hand, if the number of hidden layers is too complex, the model can be overfitted, and the model may not converge. Hence, the optimum number of hidden layers was minimized using the trial-and-error method; the number of neurons in the hidden layer was varied from 1 to 60, and the minimum mean square error (MSE) value was chosen as the final value (33 neurons). The distribution of the MSE with no of neurons in the hidden layer is shown in Fig. 15(b).

$$\text{MSE} = \frac{1}{n} \sum_{i=1}^n (e_i - c_i)^2 \quad (\text{Eq 37})$$

Before training the neural network, the input and output data should be normalized in the range of 0.1 to 0.9 to improve the convergence speed and accuracy of the ANN model. For this purpose, the following equation was used: (Ref 49)

$$X_N = 0.1 + 0.8 \times \left(\frac{X - X_{\min}}{X_{\max} - X_{\min}} \right) \quad (\text{Eq 38})$$

Here, X_N is the normalized data, X_{\min} and X_{\max} are minimum and maximum values of data, respectively, and X is the original data. The ANN computations were performed using the neural network toolbox in “MATLAB R2022b” software. The optimal epoch (one pass through input–output pair during training) was observed to be approximately 700.

The flow behavior of additively manufactured AlSi10Mg alloy over a wide range of strain rates and temperatures is predicted using optimal parameters. The predictive capability of the ANN model for training, validation, and test set is shown in Fig. 15(c), (d), and (e), respectively. Figure 16 shows good agreement between experimental and predicted flow stress

using the ANN model. The ANN model shows excellent capability in predicting the effect of thermal softening, strain rate hardening, and strain hardening on the flow stress behavior of laser powder bed fusion fabricated AlSi10Mg.

4. Discussion

4.1 Prediction Capability

The prediction capability of different models was analyzed and compared using average absolute relative error (AARE) and coefficient of correlation. The distribution of AARE in different models for the whole range of deformation conditions (temperature and strain rate) is shown in Fig. 17. The Johnson–Cook (JC) model was observed to be the least suited model for predicting the hot deformation behavior. JC model shows very poor accuracy at high-temperature range (250–300 °C), with maximum AARE reaching 23.8%. The average AARE and R^2 were observed to be 8.4% and 0.904, respectively. The JC model consists of three independent terms predicting the effect of strain hardening, thermal softening, and strain rate hardening. The JC model suffers from poor prediction capability in the materials with strong interdependency of strain rate and temperature. This might be the reason behind the poor accuracy of the original JC model in current study. The experimental stresses are correlated with predicted stresses using different models and are shown in Fig. 18. The red line shows the perfect prediction by the model. The modified Johnson–Cook (m-JC) and modified Zerilli–Armstrong (m-ZA) models have shown a maximum average absolute relative error (AARE) of 9.8% and 8.2%, respectively. Additionally, they exhibit an average AARE of 5% and 5.1%, respectively, along with R^2 values of 0.946 and 0.932, respectively. The higher accuracy of the m-JC

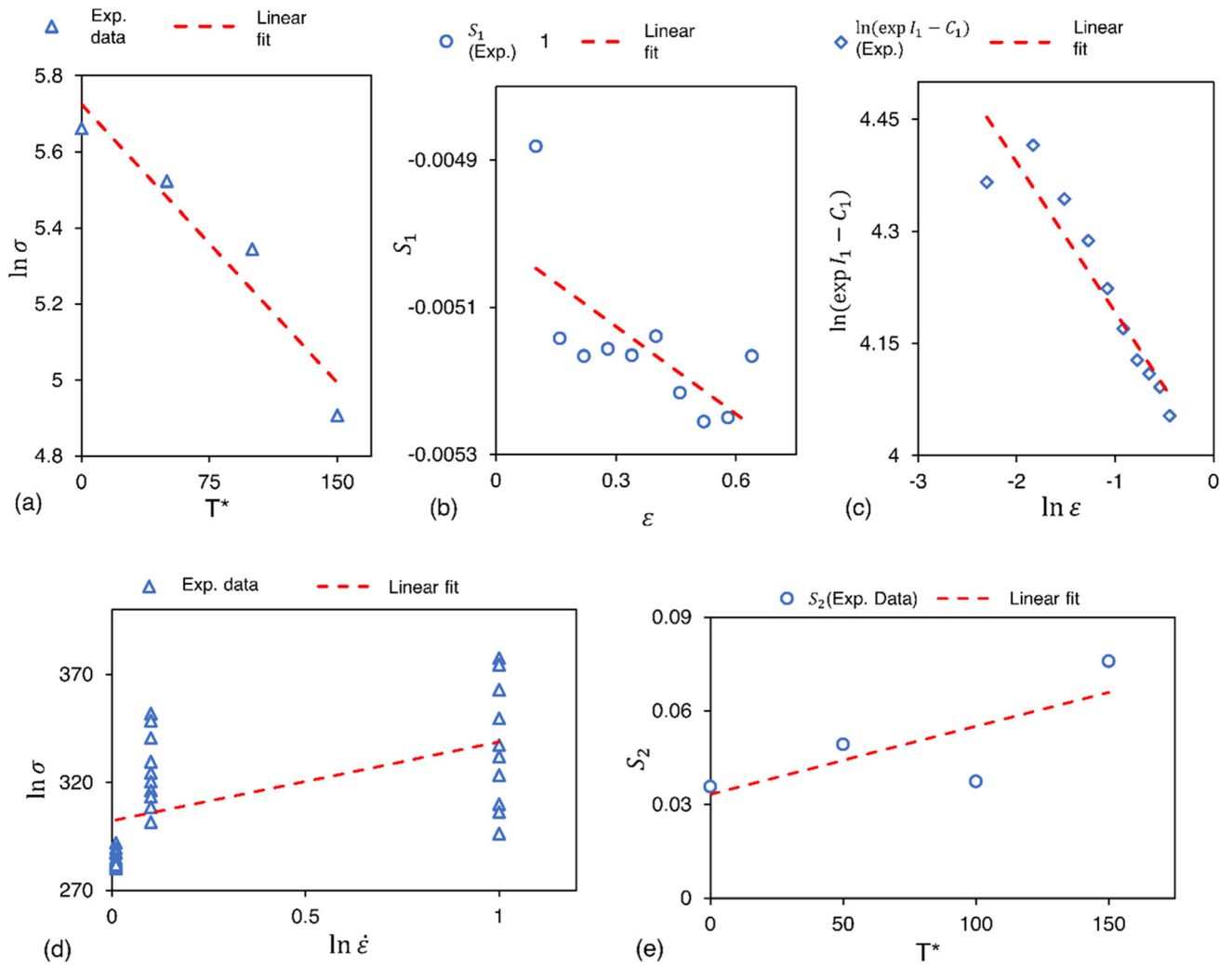


Fig. 13 Linear fit between (a) $\ln \sigma$ and T^* for a strain of 0.1, (b) slope S_1 and ε , (c) $\ln(\exp I_1 - C_1)$ and $\ln \varepsilon$, (d) $\ln \sigma$ and $\ln \dot{\varepsilon}$ for temperature of 150°C, and (e) slope S_2 , and T^*

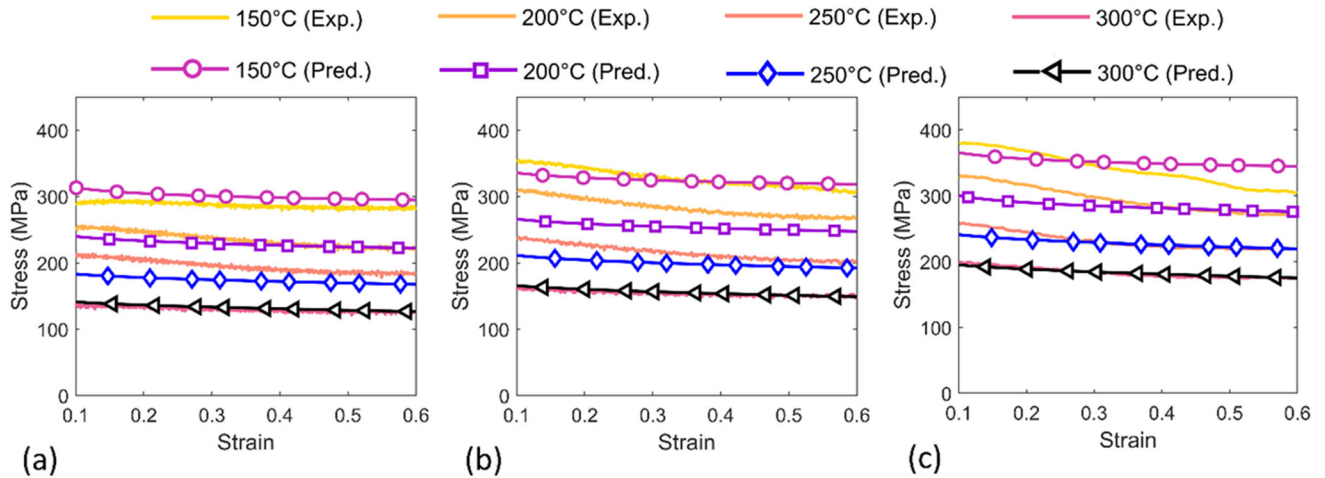


Fig. 14 Comparison between experimental and predicted stress–strain curves by modified Zerilli–Armstrong model (a) 0.01 s⁻¹, (b) 0.1 s⁻¹, (c) 1 s⁻¹

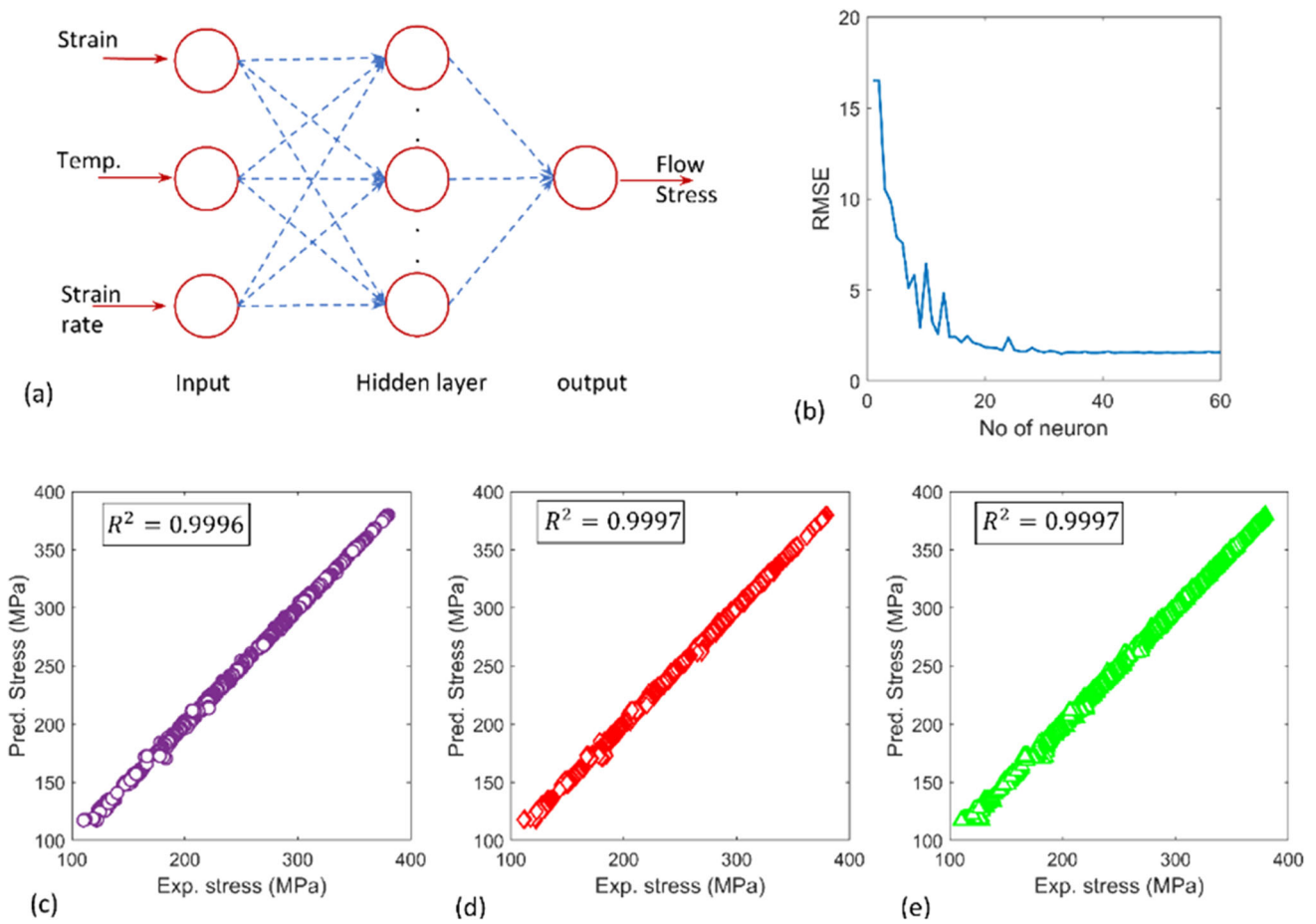


Fig. 15 (a) schematic diagram of the ANN model, (b) Variation in RMSE with no of neuron in the hidden layer, the predictive capability of ANN for (c) Training set, (d) test set, (e) validation set

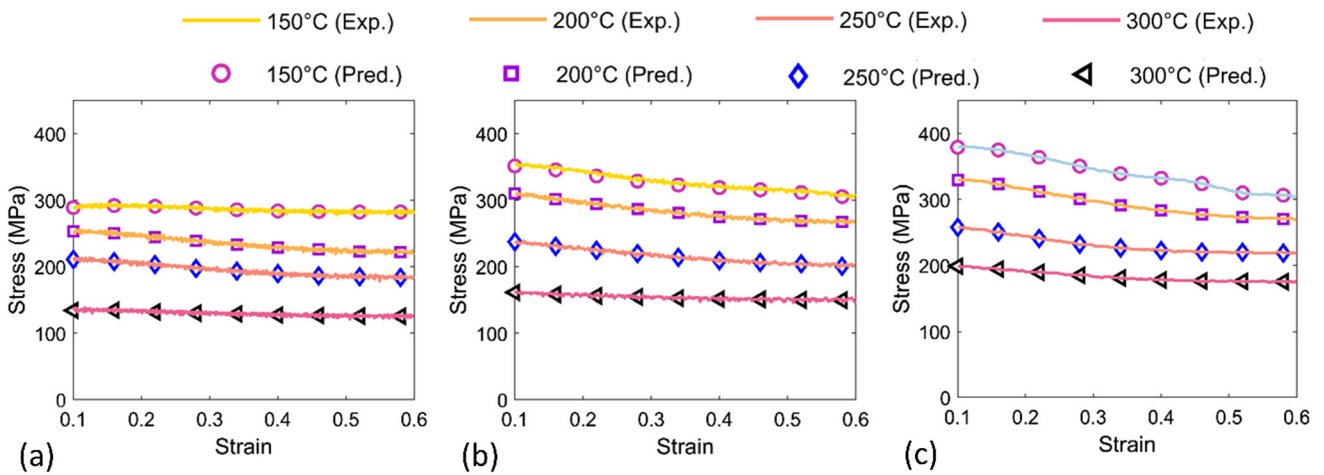


Fig. 16 Comparison between experimental and predicted stress–strain curves by modified Zerilli–Armstrong model (a) 0.01 s^{-1} , (b) 0.1 s^{-1} , (c) 1 s^{-1}

and m-ZA models compared to the original JC model might be attributed to the coupled effect of temperature and strain rate in both models. The modified Fields–Backofen model (m-FB) and strain-compensated Arrhenius equation (SCAE) were the best-suited phenomenological models for predicting the hot defor-

mation behavior of additively manufactured AlSi10Mg. m-FB and SCAE models show similar accuracy, with m-FB offering slightly better accuracy compared to the SCAE (maximum AARE of 5.6% in SCAE compared to 6.4% in m-FB, and average AARE of 3.3% in m-FB compared to 3.9% in SCAE).

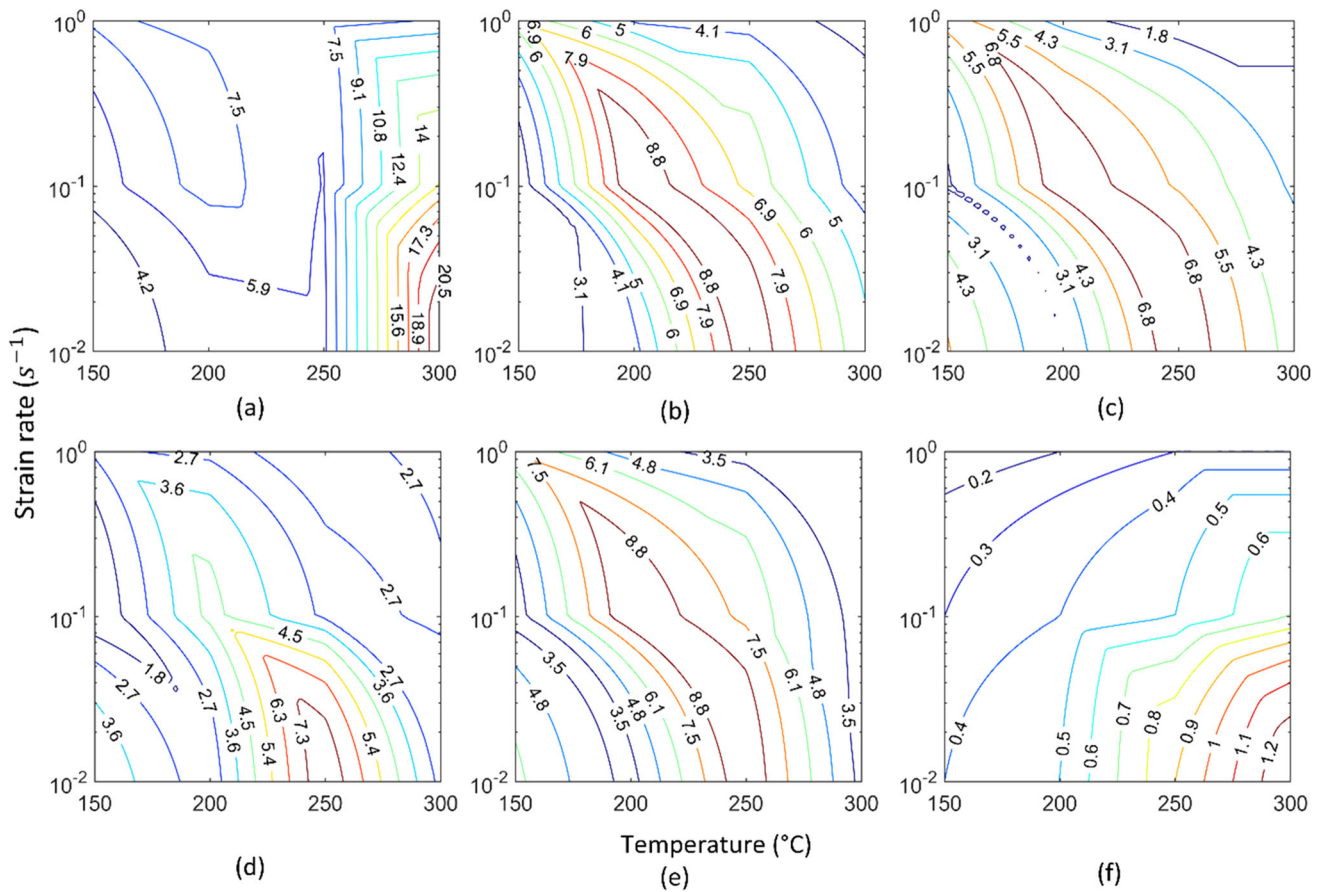


Fig. 17 Distribution of AARE in (a) JC, (b) m-JC, (c) SCAE, (d) m-FB, (e) m-ZA, (f) ANN (number in contour lines represent the average error in %)

The ANN network offers better prediction capability compared to the phenomenological model. The AARE and R^2 value of the ANN network were observed to be 0.5% and 0.999, respectively. The ANN network offers the unique advantage of not having any pre-defined mathematical model, and hence, it can be precisely fitted for the individual problem. However, the ANN network cannot provide any insight into the flow stress behavior during hot deformation.

4.2 Interpolation and Extrapolation Capabilities

The interpolation refers to the capability of the model to predict the flow stress within the input range of the model, whereas the extrapolation refers to the prediction capability of the model outside the training range of the model. The capacity of models to perform interpolation and extrapolation of experimental data is crucial for minimizing the time and experimental resources. The investigation into the interpolation accuracy involved training different models at strain rates of ($0.01s^{-1}$, $0.1s^{-1}$, and $1s^{-1}$) and temperatures of (150 °C, 250 °C, and 300 °C); the models were subsequently tested for their ability to predict the flow stress behavior at strain rates of ($0.01s^{-1}$, $0.1s^{-1}$, and $1s^{-1}$) and a temperature of 200 °C. Similarly, the extrapolation accuracy was assessed by training the models at strain rates of ($0.01s^{-1}$, $0.1s^{-1}$, and $1s^{-1}$), and temperature of (150 °C, 200 °C, and 250 °C), and subsequently testing the models for strain rate of ($0.01s^{-1}$, $0.1s^{-1}$, and $1s^{-1}$), and a temperature of 300 °C. The

prediction capability of different models for extrapolation and interpolation is shown in Fig. 19.

The accuracy for interpolation is good for both phenomenological models and the ANN model, and the ANN model has better interpolation capabilities compared to the phenomenological models. On the other hand, the extrapolation capabilities of the ANN were observed to be poor compared to the phenomenological models such as SCAE and m-FB. The extrapolation is inherently risky compared to the interpolation as the material behavior can vary significantly beyond the tested range of temperature and strain rate. However, the accuracy of the phenomenological model remains consistent within the appropriate range outside the tested conditions. The higher accuracy of the phenomenological model can be attributed to the fixed mathematical form of the models, and the poor accuracy of the ANN model for extrapolation might be accredited to the absence of the fixed mathematical form.

4.3 Operational Ease

The operational ease pertains to the user-friendliness of the models. Simplicity and robustness are the critical factors for practical applications in the industries. The usability of the models is assessed based on the number of parameters, whereas the robustness of the model is determined by the repeatability and reproducibility of the results. The number of constants for different models is shown in Table 9. The SCAE and m-FB models offer similar overall accuracy; however, the m-FB only has 10 model constants compared to the 24 model constants in

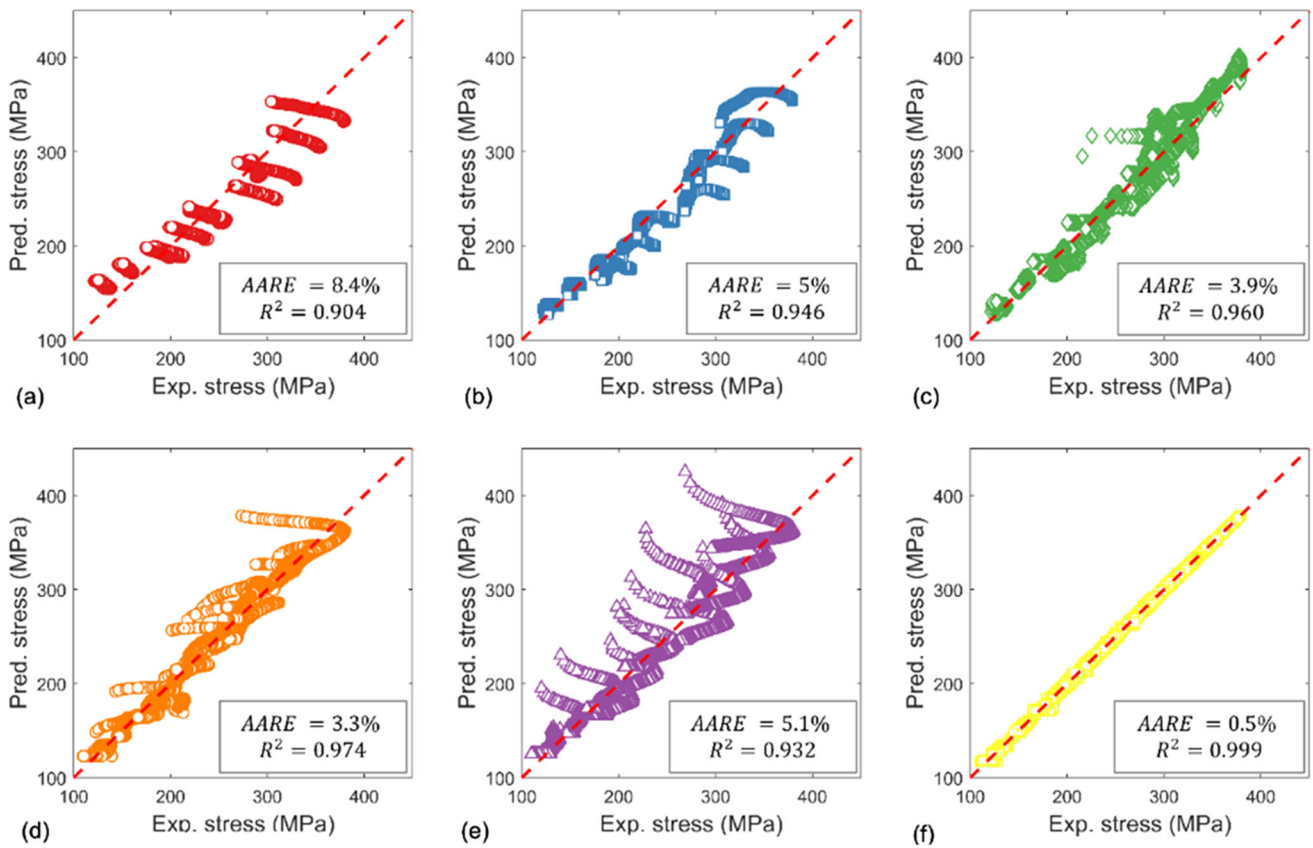


Fig. 18 Linear fit between predicted and experimental flow stress in (a) JC, (b) m-JC, (c) SCAE, (d) m-FB, (e) m-ZA, (f) ANN

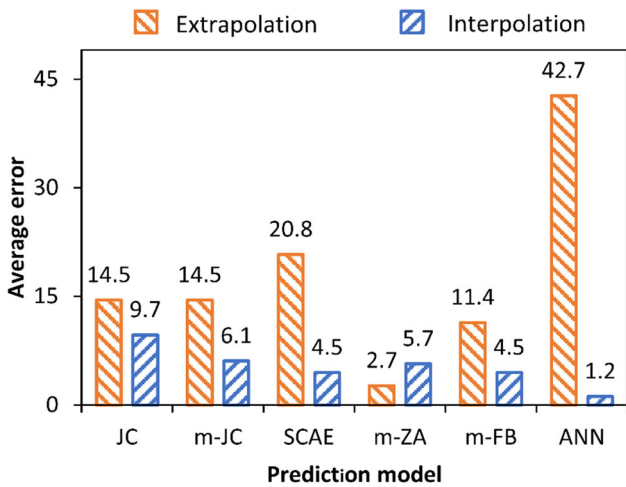


Fig. 19 (a) Prediction capability of different models for interpolation and extrapolation

the SCAE models. This indicates that the m-FB models should be preferred over the SCAE model for industrial applications. The robustness of the model refers to the repeatability of the models; the phenomenological models are very robust as a consequence of their mathematical form. On the other hand, the ANN model, despite having high accuracy, is not very robust as it can be system- and operator-dependent.

5. Conclusions

The deformation behavior of additively manufactured AlSi10Mg was predicted and analyzed using different phenomenological models and artificial neural networks (ANN). The flow stress in the current investigation follows the usual trend observed in the aluminum alloy. The flow stress decreases with an increase in the temperature and a decrease in strain rate. Different phenomenological models, such as JC, m-JC, SCAE, m-ZA, m-FB, and ANN, were used to investigate the flow behavior of additively manufactured AlSi10Mg. The JC model was observed to be the least-suited method for predicting hot deformation behavior in current study. The original JC model offers an average AARE of 8% and a maximum AARE of 28%. The m-FB model and SCAE model were observed to be the best-suited phenomenological models for prediction of flow stress. The m-FB was observed to be marginally better compared to the SCAE model (average AARE of 3.3% in m-FB compared to 3.9% in SCAE, and maximum AARE of 5.6% in SCAE compared to 6.4% in m-FB). The m-FB model offers the best overall performance in terms of overall accuracy, interpolation, and extrapolation capability and a low number of constants. The ANN network does not have a definite mathematical model and hence can be precisely fitted for the individual problem. The ANN network offered the highest overall prediction capability with an AARE and correlation coefficient of 0.5% and 0.999, respectively.

Table 9 Comparison of different models for flow stress prediction

	JC	m-JC	SCAE	m-FB	m-ZA	ANN
AARE (%), overall	8.4	5	3.9	3.3	5.1	0.5
R^2	0.904	0.946	0.960	0.974	0.932	0.999
AARE (%), extrapolation	14.5	14.5	20.8	2.7	11.4	42.7
AARE (%), Interpolation	9.7	6.1	4.5	5.7	4.5	1.2
No of constants	5	6	24	10	7	N/A

Conflict of interest

All the studies performed in the manuscript are genuine and original. There is no conflict of interest, as per our knowledge.

References

- R. Motallebi, Z. Savaedi, and H. Mirzadeh, Additive Manufacturing—A Review of Hot Deformation Behavior and Constitutive Modeling of Flow Stress, *Curr. Opin. Solid State Mater. Sci.*, 2022, **26**(3), p 100992. <https://doi.org/10.1016/j.cossms.2022.100992>
- A. Raja, S.R. Cheethirala, P. Gupta, N.J. Vasa, and R. Jayaganthan, A Review on the Fatigue Behaviour of AlSi10Mg Alloy Fabricated using Laser Powder Bed Fusion Technique, *J. Mater. Res. Technol.*, 2022, **17**, p 1013-1029
- M. Hoffmann and A. Elwany, In-Space Additive Manufacturing: A Review, *J. Manuf. Sci. Eng.*, 2023, **145**(2), p 020801
- Z. Wang, R. Ummethala, N. Singh, S. Tang, C. Suryanarayana, J. Eckert, and K.G. Prashanth, Selective Laser Melting of Aluminum and Its Alloys, *Materials*, 2020, **13**(20), p 1-67
- T. Hirata, T. Kimura, and T. Nakamoto, Effects of Hot Isostatic Pressing and Internal Porosity on the Performance of Selective Laser Melted AlSi10Mg Alloys, *Mater. Sci. Eng. A*, 2019, **2020**, p 772
- S.R. Ch, A. Raja, P. Nadig, R. Jayaganthan, and N.J. Vasa, Influence of Working Environment and Built Orientation on the Tensile Properties of Selective Laser Melted AlSi10Mg Alloy, *Mater. Sci. Eng. A*, 2019, **750**, p 141-151. <https://doi.org/10.1016/j.msea.2019.01.103>
- S. Beretta, More than 25 Years of Extreme Value Statistics for Defects: Fundamentals, Historical Developments, Recent Applications, *Int. J. Fatigue*, 2021, **151**, p 106407
- M. Bambach, I. Sizova, J. Szyndler, J. Bennett, G. Hyatt, J. Cao, T. Papke, and M. Merklein, On the Hot Deformation Behavior of Ti-6Al-4V Made by Additive Manufacturing, *J. Mater. Process. Technol.*, 2020, **2021**(288), p 116840. <https://doi.org/10.1016/j.jmatprotec.2020.116840>
- A. Tiwari, G. Singh, and R. Jayaganthan, Improved Corrosion Resistance Behaviour of AlSi10Mg Alloy Due to Selective Laser Melting, *Coatings*, 2023, **13**(2), p 225
- A. Elkholy, P. Quinn, S.M. Uí Mhurchadha, R. Raghavendra, and R. Kempers, Characterization and Analysis of the Thermal Conductivity of AlSi10Mg Fabricated by Laser Powder Bed Fusion, *J. Manuf. Sci. Eng.*, 2022, **144**(10), p 101001
- P. He, H. Kong, Q. Liu, M. Ferry, J.J. Kruzic, and X. Li, Elevated Temperature Mechanical Properties of TiCN Reinforced AlSi10Mg Fabricated by Laser Powder Bed Fusion Additive Manufacturing, *Mater. Sci. Eng. A*, 2020, **2021**(811), p 141025. <https://doi.org/10.1016/j.msea.2021.141025>
- S. Rosenthal, M. Hahn, and A.E. Tekkya, Deep Drawability of Additively Manufactured Sheets with a Structured Core, *Int. J. Mater. Form.*, 2023, **16**(2), p 1-15
- A.K. Maurya, J.T. Yeom, S.W. Kang, C.H. Park, J.K. Hong, and N.S. Reddy, Optimization of Hybrid Manufacturing Process Combining Forging and Wire-Arc Additive Manufactured Ti-6Al-4V through Hot Deformation Characterization, *J. Alloys Compd.*, 2022, **894**, p 162453. <https://doi.org/10.1016/j.jallcom.2021.162453>
- I. Sizova, A. Sviridov, M. Bambach, M. Eisentraut, S. Hemes, U. Hecht, A. Marquardt, and C. Leyens, A Study on Hot-Working as Alternative Post-Processing Method for Titanium Aluminides Built by Laser Powder Bed Fusion and Electron Beam Melting, *J. Mater. Process. Technol.*, 2020, **2021**(291), p 117024. <https://doi.org/10.1016/j.jmatprotec.2020.117024>
- C.I. Pruncu, C. Hopper, P.A. Hooper, Z. Tan, H. Zhu, J. Lin, and J. Jiang, Study of the Effects of Hot Forging on the Additively Manufactured Stainless Steel Preforms, *J. Manuf. Process.*, 2020, **57**(July), p 668-676. <https://doi.org/10.1016/j.jmapro.2020.07.028>
- P. Snopiński, K. Matus, F. Tatiček, and S. Ruzs, Overcoming the Strength-Ductility Trade-off in Additively Manufactured AlSi10Mg Alloy by ECAP Processing, *J. Alloys Compd.*, 2022, **918**, p 165817
- A. Hosseinzadeh, A. Radi, J. Richter, T. Wegener, S.V. Sajadifar, T. Niendorf, and G.G. Yapici, Severe Plastic Deformation as a Processing Tool for Strengthening of Additive Manufactured Alloys, *J. Manuf. Process.*, 2021, **68**, p 788-795. <https://doi.org/10.1016/j.jmapro.2021.05.070>
- W. Shen, F. Xue, C. Li, Y. Liu, X. Mo, and Q. Gao, Study on Constitutive Relationship of 6061 Aluminum Alloy Based on Johnson-Cook Model, *Mater. Today Commun.*, 2023, **37**, p 106982. <https://doi.org/10.1016/j.mtcomm.2023.106982>
- S. Gairola, G. Singh, R. Jayaganthan, and J. Ajay, High Temperature Performance of Additively Manufactured Al 2024 Alloy: Constitutive Modelling, Dynamic Recrystallization Evolution and Kinetics, *J. Mater. Res. Technol.*, 2023, **25**, p 3425-3443. <https://doi.org/10.1016/j.jmrt.2023.06.102>
- S.C. Krishna, S. Anoop, N.T.B.N. Koundinya, N.K. Karthick, P. Muneshwar, and B. Pant, Constitutive Modelling of Hot Deformation Behaviour of Nitrogen Alloyed Martensitic Stainless Steel, *Trans. Indian Natl. Acad. Eng.*, 2020, **5**(4), p 769-777. <https://doi.org/10.1016/s41403-020-00182-y>
- B. Li, Y. Duan, S. Zheng, M. Peng, M. Li, and H. Bu, Microstructural and Constitutive Relationship in Process Modeling of Hot Working: The Case of a 60Mg-30Pb-9.2Al-0.8B Magnesium Alloy, *J. Mater. Res. Technol.*, 2023, **26**, p 9139-9156
- Y. Sun, L. Bao, and Y. Duan, Hot Compressive Deformation Behaviour and Constitutive Equations of Mg-Pb-Al-1B-0.4Sc Alloy, *Philos. Mag.*, 2021, **101**(22), p 2355-2376. <https://doi.org/10.1080/14786435.2021.1974113>
- W. Bao, L. Bao, D. Liu, D. Qu, Z. Kong, M. Peng, and Y. Duan, Constitutive Equations, Processing Maps, and Microstructures of Pb-Mg-Al-B-0.4Y Alloy under Hot Compression, *J. Mater. Eng. Perform.*, 2020, **29**(1), p 607-619. <https://doi.org/10.1007/s11665-019-04544-8>
- J. Cai, K. Wang, and Y. Han, A Comparative Study on Johnson Cook, Modified Zerilli-Armstrong and Arrhenius-Type Constitutive Models to Predict High-Temperature Flow Behavior of Ti-6Al-4V Alloy in $\alpha + \beta$ Phase, *High Temp. Mater. Process.*, 2016, **35**(3), p 297-307
- W. Jia, S. Xu, Q. Le, L. Fu, L. Ma, and Y. Tang, Modified Fields-Backofen Model for Constitutive Behavior of as-Cast AZ31B Magnesium Alloy during Hot Deformation, *Mater. Des.*, 2016, **106**, p 120-132
- Y. Duan, L. Ma, H. Qi, R. Li, and P. Li, Developed Constitutive Models, Processing Maps and Microstructural Evolution of Pb-Mg-10Al-0.5B Alloy, *Mater. Charact.*, 2017, **129**(April), p 353-366. <https://doi.org/10.1016/j.matchar.2017.05.026>
- S.A. Sani, G.R. Ebrahimi, H. Vafaenezhad, and A.R. Kiani-Rashid, Modeling of Hot Deformation Behavior and Prediction of Flow Stress in a Magnesium Alloy using Constitutive Equation and Artificial Neural Network (ANN) Model, *J. Magnes. Alloy.*, 2018, **6**(2), p 134-144. <https://doi.org/10.1016/j.jma.2018.05.002>
- X. Li, J. Wang, J. Ma, T. Yang, S. Yuan, X. Liu, Y. Feng, and P. Jin, Thermal Deformation Behavior of Mg-3Sn-1Mn Alloy Based on Constitutive Relation Model and Artificial Neural Network, *J. Mater.*

- Res. Technol.*, 2023, **24**, p 1802-1815. <https://doi.org/10.1016/j.jmrt.2023.03.096>
29. K.A. Babu and S. Mandal, Regression Based Novel Constitutive Analyses to Predict High Temperature Flow Behavior in Super Austenitic Stainless Steel, *Mater. Sci. Eng. A*, 2017, **703**(July), p 187-195. <https://doi.org/10.1016/j.msea.2017.07.035>
 30. Y.C. Lin and X.M. Chen, A Critical Review of Experimental Results and Constitutive Descriptions for Metals and Alloys in Hot Working, *Mater. Des.*, 2011, **32**(4), p 1733-1759
 31. P. Tao, J. Zhong, H. Li, Q. Hu, S. Gong, and Q. Xu, Microstructure, Mechanical Properties, and Constitutive Models for Ti-6Al-4V Alloy Fabricated by Selective Laser Melting (SLM), *Metals*, 2019, **9**(4), p 447
 32. Y. Niu, Z. Sun, Y. Wang, and J. Niu, Phenomenological Constitutive Models for Hot Deformation Behavior of Ti6Al4V Alloy Manufactured by Directed Energy Deposition Laser, *Metals*, 2020, **10**(11), p 1496
 33. H. Mirzadeh, A Simplified Approach for Developing Constitutive Equations for Modeling and Prediction of Hot Deformation Flow Stress, *Metall. Mater. Trans. A*, 2015, **46**, p 4027-4037
 34. H. Rastegari, M. Rakhshkhorshid, M.C. Somani, and D.A. Porter, Constitutive Modeling of Warm Deformation Flow Curves of an Eutectoid Steel, *J. Mater. Eng. Perform.*, 2017, **26**, p 2170-2178
 35. M. Shalbafi, R. Roumina, and R. Mahmudi, Hot Deformation of the Extruded Mg-10Li-1Zn alloy: Constitutive Analysis and Processing Maps, *J. Alloys Compd.*, 2017, **696**, p 1269-1277
 36. ASTM E209-18, Standard Practice for Compression Tests of Metallic Materials at Elevated Temperatures with Conventional or Rapid Heating Rates and Strain Rates, *Annual Book of ASTM Standards*, 2010
 37. A. Shokry, S. Gowid, and G. Kharmanda, An Improved Generic Johnson–Cook Model for the Flow Prediction of Different Categories of Alloys at Elevated Temperatures and Dynamic Loading Conditions, *Mater. Today Commun.*, 2021, **27**, p 102296
 38. S.R. Ch, A. Raja, R. Jayaganthan, N.J. Vasa, and M. Raghunandan, Study on the Fatigue Behaviour of Selective Laser Melted AlSi10Mg Alloy, *Mater. Sci. Eng. A*, 2019, **2020**(781), p 139180. <https://doi.org/10.1016/j.msea.2020.139180>
 39. G.R. Johnson and W.H. Cook, A Computational Constitutive Model and Data for Metals Subjected to Large Strain, High Strain Rates and High Pressures, *Seventh Int. Symp. Ballist.*, p 541-547 (1983)
 40. S. Liu, H. Zhu, G. Peng, J. Yin, and X. Zeng, Microstructure Prediction of Selective Laser Melting AlSi10Mg using Finite Element Analysis, *Mater. Des.*, 2018, **142**, p 319-328. <https://doi.org/10.1016/j.matdes.2018.01.022>
 41. Y.C. Lin, X.M. Chen, and G. Liu, A Modified Johnson–Cook Model for Tensile Behaviors of Typical High-Strength Alloy Steel, *Mater. Sci. Eng. A*, 2010, **527**(26), p 6980-6986
 42. A. Shokry, S. Gowid, H. Mulki, and G. Kharmanda, On the Prediction of the Flow Behavior of Metals and Alloys at a Wide Range of Temperatures and Strain Rates using Johnson–Cook and Modified Johnson–Cook-Based Models: A Review, *Materials*, 2023, **16**(4), p 1574
 43. C.M. Sellars and W.J. McTegart, On the Mechanism of Hot Deformation, *Acta Metall.*, 1966, **14**(9), p 1136-1138
 44. Y.Q. Cheng, H. Zhang, Z.H. Chen, and K.F. Xian, Flow Stress Equation of AZ31 Magnesium Alloy Sheet during Warm Tensile Deformation, *J. Mater. Process. Technol.*, 2008, **208**(1-3), p 29-34
 45. F.J. Zerilli and R.W. Armstrong, Dislocation-Mechanics-Based Constitutive Relations for Material Dynamics Calculations, *J. Appl. Phys.*, 1987, **61**(5), p 1816-1825. <https://doi.org/10.1063/1.338024>
 46. D. Samantaray, S. Mandal, U. Borah, A.K. Bhaduri, and P.V. Sivaprasad, A Thermo-Viscoplastic Constitutive Model to Predict Elevated-Temperature Flow Behaviour in a Titanium-Modified Austenitic Stainless Steel, *Mater. Sci. Eng. A*, 2009, **526**(1-2), p 1-6
 47. R.S. Haridas, P. Agrawal, S. Thapliyal, S. Yadav, R.S. Mishra, B.A. McWilliams, and K.C. Cho, Strain Rate Sensitive Microstructural Evolution in a TRIP Assisted High Entropy Alloy: Experiments, Microstructure and Modeling, *Mech. Mater.*, 2021, **156**, p 103798. <https://doi.org/10.1016/j.mechmat.2021.103798>
 48. Q. Qin, M.L. Tian, and P. Zhang, Investigation of a Coupled Arrhenius-Type/Rossard Equation of AH36 Material, *Materials*, 2017, **10**(4), p 407
 49. H. Mirzadeh, J.M. Cabrera, and A. Najafizadeh, Modeling and Prediction of Hot Deformation Flow Curves, *Metall. Mater. Trans. A*, 2012, **43**, p 108-123

Publisher's Note Springer Nature remains neutral with regard to jurisdictional claims in published maps and institutional affiliations.

Springer Nature or its licensor (e.g. a society or other partner) holds exclusive rights to this article under a publishing agreement with the author(s) or other rightsholder(s); author self-archiving of the accepted manuscript version of this article is solely governed by the terms of such publishing agreement and applicable law.